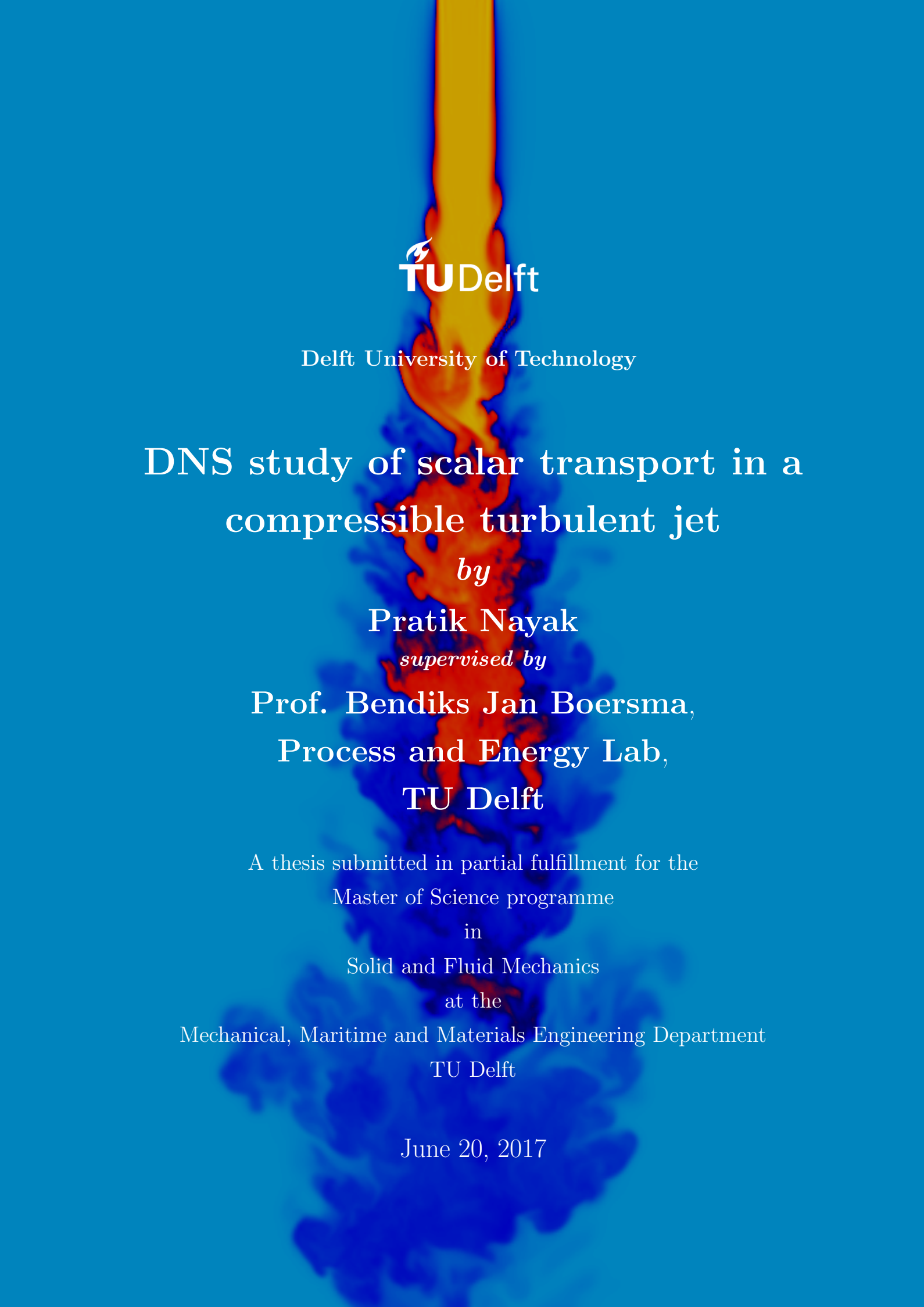

Delft University of Technology

DNS study of scalar transport in a compressible turbulent jet

by

Pratik Nayak

supervised by

Prof. Bendiks Jan Boersma,

Process and Energy Lab,

TU Delft

A thesis submitted in partial fulfillment for the
Master of Science programme
in
Solid and Fluid Mechanics
at the
Mechanical, Maritime and Materials Engineering Department
TU Delft

June 20, 2017

"God put me on this earth to accomplish a certain number of things. Right now, I am so far behind, I will never die."

Bill Watterson.

"The more I read, the more I acquire, the more certain I am that I know nothing."

Voltaire.

"The human brain is finite. The powers of its imagination, infinite."

Acknowledgements

I would like to thank Prof. Bendiks Jan Boersma for his guidance, support and invaluable discussions throughout this thesis.

I would like to thank my parents for their unconditional support and encouragement. I would also like to thank Amitosh Dash, Shrinivas Chimmalgi and Vadiraj Patil for their review and feedback on the thesis report.

Last but not the least, I would like to thank the Delft Wind Energy Institute (DUWIND) for giving me an opportunity to study at TU Delft by supporting me through their scholarship. I am extremely grateful to them.

Contents

List of Figures

List of Tables

Abbreviations

Acronym	**W***hat (it)* **S***tands* **F***or*
NSF	**N***avier–***S***tokes–***F***ourier*
DNS	**D***irect* **N***umerical* **S***imulation*
LES	**L***arge* **E***ddy* **S***imulation*
RANS	**R***eynolds* **A***veraged* **N***avier* **S***tokes*
Cfd	**C***ompact* **f***inite* **d***ifference*
ENO	**E***ssentially* **N***on-***O***scillatory*
WENO	**W***eighted* **E***ssentially* **N***on-***O***scillatory*
RK4	**R***unge-***K**utta* **4***th order*

Symbols

Symbol	***Name and Usage***
∇	Gradient operator
$\nabla\cdot$	Divergence operator
$\frac{\partial}{\partial i}$	Partial derivative with respect to the variable i
Ω	Boundary of the grid
μ	Dynamic viscosity of fluid
Re	Reynolds Number
Pr	Prandtl Number
Sc	Schmidt Number
p	Pressure
$\mathbf{u} = (u, v, w)$	Velocity vector
ρ	Density
e	Total energy
Y_k	Scalar concentration of the k-th species

Chapter 1

Introduction

1.1 Abstract

Direct Numerical simulations (DNS) belong to the class of simulations that strive to emulate the real physical flow by trying to simulate the complete range of scales involved in the flow. Though the computational power has steadily increased in the past few decades, resolving the complete range of scales from the largest scales up to the Kolmogorov scales can be very complicated and time consuming for moderately high Reynolds numbers as well. Hence, DNS is still expected to be a research tool to study relatively simple flows and geometries for the forseeable future unlike its counterparts such as Large Eddy Simulations (LES) and Reynolds Averaged Navier–Stokes (RANS) methods. The main objective of DNS studies is to study the flows so that turbulence models which are parametrized can be improved upon with the physical insight from the results of DNS. It also helps in studying the effect of numerical methods and techniques applicable to real flows and their stand-alone effects without any type of modeling as done for LES or RANS.

This thesis is concerned with the DNS study of a compressible turbulent jet. A turbulent jet belongs to the class of free turbulent flows, in the sense that, it is not bounded physically. In this thesis, the transport of a passive scalar through the jet is studied. At higher Reynolds numbers, for convection dominated equations such as the scalar transport equation, discontinuities can occur due to the hyperbolic nature of the equations. When central methods are used, oscillations are observed in the regions of the discontinuities. These oscillations can make the solution unphysical. Therefore, in this thesis

the scalar transport equation has been modeled with an additional Weighted Essentially Non-Oscillatory (WENO) interpolation to accurately capture the discontinuities without oscillations. The WENO interpolation is combined with central compact finite difference methods to reduce the numerical dissipation while maintaining the order of accuracy in the smooth regions which is essential in high Reynolds number flows.

It was observed that a high dissipation setting for the WENO interpolation removed the oscillations but introduced artificial numerical viscosity. Therefore a relatively large domain was used with a low dissipation which while removing the oscillations and reducing the numerical dissipation. The WENO method for the compressible turbulent jet was first validated with experimental results to ascertain the accuracy of the grid resolution. The same grid resolution was used to study some properties of the jet at two different Schmidt numbers at a slightly lower Reynolds number. It was observed that the results obtained with the WENO interpolation matched well with the experimental results while being physical valid solutions because they had no oscillations. The results also showed different modes of instabilities for different Schmidt numbers and that the decay rate is a good characterization of the properties of the turbulent jet.

In conclusion, the WENO methods can be a very helpful method to accurately capture the discontinuities in an efficient manner and is also suitable for methods such as LES and RANS to model flows that have some hyperbolic nature of terms in the governing equations.

1.2 Motivation and Literature

Turbulent jets are encountered in many engineering applications including jet engine exhausts, rocket exhausts, industrial processes and the like. They are also a part of many turbulent combustion processes. Therefore, it is important to understand the flow physics and the characteristics to be able to obtain the correct jet properties for the specific application. Being a free flow, they become turbulent at relatively small Reynolds numbers. Many studies have been performed to study the properties of a jet [3, 4] and also to study the acoustics related to the jets [5–8], which is important for aerospace applications.

Scalar transport in turbulent jets is of importance in turbulent combustion and in exhausts where fuel and oxidizer combust to produce exhaust gases. It is also important

in applications where a scalar is transported through a jet but is non-reactive. Many studies have been performed to study the transport of a scalar [3, 9] but mainly in either axis-symmetric or for simplified round jets. This thesis aims to study the scalar transport in a compressible turbulent jet for moderate to high Reynolds numbers to accurately capture the discontinuities and minimize numerical dissipation while doing so.

The scalar transport equation is essentially an advection-diffusion equation and hence is a combination of hyperbolic and parabolic type pde's, the advective terms giving it the hyperbolic nature and the diffusive term giving it the parabolic nature. In nature, all disturbances travel at a certain speed that is restricted by the speed of light. Therefore, in all the processes, the information travels at a certain speed and is never instantaneous. The main feature of hyperbolic pde's are that they model processes that travel at certain(wave) speeds and in a characteristic sense, that means that a discontinuity (a sudden change in a certain property) travels at the characteristic speed of the respective wave.

Different authors have observed that when these hyperbolic pde's with large characteristic speeds are modeled using central methods (methods taking information from both sides of the discontinuity), oscillations are observed which can make the solution unphysical [4]. Therefore, to remove these oscillations a different class of methods must be used. The class of methods that have been used in this thesis are called the WENO methods, Weighted Essentially Non-Oscillatory methods. They are an improvement of the ENO (Essentially Non-Oscillatory) methods first introduced by Harten et.al [10]. The idea was to consider many candidate stencils rather than one stencil and measure "smoothness" of the function in the stencils and choose the stencil in which the function is the "smoothest" in some sense. These class of methods were very effective for problems that contained discontinuities but were dissipative. This made the methods quite popular. Various researchers worked to improve the ENO methods to improve the measuring of smoothness and the choosing of stencils [11–13]. It was recognized by Liu, Osher and Chan [14] that instead of choosing a smoothest stencil, one could choose a convex combination of all the stencils thereby giving a weight to each of the stencils depending on the smoothness of the function in the respective stencils. These methods were called the WENO methods. Jiang and Shu [15] did an extensive study of the methods and gave a new method to estimate the smoothness indicators which was more efficient and robust than the divided difference methods used in the previous ENO methods. This smoothness indicator was based on the measurement of the Total variation of the function in the stencil and are extensively used in almost all WENO

and WENO derived methods today. An added advantage of the WENO methods was that the convex combination of the stencils increased the accuracy in the smooth regions as explained in [15] while capturing discontinuities and reverting to the normal order in the regions of discontinuities. This was not possible in ENO because only a single stencil was chosen and hence the maximum order even in the smooth regions was limited.

With WENO, many improvements were still possible. The numerical dispersion was still quite high enough that the resolution of short waves was not good enough. Tam and Webb [16] developed dispersion relation preserving schemes that were suitable for aero-acoustics simulations where even the capture of small disturbances was important. Martin et.al [17] developed schemes that were optimal based on the bandwidth and suitable for compressible turbulent flows. Another aspect of the WENO schemes were that they were still quite dissipative. Due to the inherent upwinding to capture the discontinuities, a lot of numerical dissipation was introduced in the schemes. This numerical dissipation is not desirable for flows that have to resolve a wide range of of scales and especially flows where the high wavenumbers play an important role. In general, dissipation can be reduced by two methods, one being the usage of a hybrid scheme, that is schemes that used sub-schemes that had lesser dissipation in the smooth regions. Adams and Sharif [18] used a hybrid version of the compact upwind and the ENO schemes as a start to these hybrid methods. Ren et.al [19] considered schemes that were a hybrid of the WENO and the compact schemes and improved the transition between the sub-schemes. The other idea was to use central symmetrical stencils. This was pursued by Martin et.al [17], but the solution degenerated near critical points. Another idea was to map the non-linear WENO weights so that they would have a lesser dissipation and better properties. This was introduced by Henrick et. al [20] and he mapped the traditional WENO schemes and obtained better properties. Finally, Liu et al.[21] pursued schemes that were a hybrid of the central compact and the WENO schemes. They used grid points on both staggered and co-located grids to calculate the derivatives of the fields. Their weighting procedure involved the usage of lower order upwind stencils as well as high order central stencils and the calculation of smoothness of the fields in these stencils to obtain, first linear weights and then non-linear weights which then formed the overall scheme. The weights, both non-linear and linear were dependent on user defined constants which are to be set based on the nature of the problem. This thesis combines these approaches to study the scalar transport in compressible turbulent jet at moderately high Reynolds numbers in an effort to remove the numerical unphysical oscillations while reducing the numerical

dissipation.

1.3 Goals and Objectives

The objectives of the project were the following:

1. Study the properties and characteristics of the turbulent jet at moderately high Reynolds and Mach numbers.
2. Identify the issues that are faced with scalar transport modeling at these moderately high Reynolds numbers.
3. Identify and implement the current existing methods to solve the problems with the scalar transport modeling.
4. Develop and implement a method to accurately model the scalar transport phenomena.
5. Compare the improvement in the model with the previous methods and report on the results.

1.4 Structure of this report

Chapter 2 explains and elaborates on the ideas and the theory that have been implemented in this thesis. It also provides a reasoning of specific methods and advantages and dis-advantages of each method wherever possible.

Chapter 3 deals with the implementation aspects and helps the reader understand the implementations of the ideas explained in Chapter 2 and concludes with some numerical tests.

Chapter 4 presents the results in the thesis starting with a validation with experiments and finally comparing flow physics for some different parameters.

Chapter 5 concludes this thesis with some results of the thesis and provides the reader with ideas for future work possible.

Chapter 2

Methodology and Ideas

This section explains the theory and ideas involved in this thesis. The governing equations are explained first which form the theoretical basis of the physics of the problem. The numerical aspects such as spatial, temporal and boundary discretizations are explained later to completely understand the implementation that has been used in this thesis.

2.1 Governing Equations

Fluid dynamics are in general governed by the Navier–Stokes (NS) equations along with other similar conservation laws such as the energy equation and the equation of state depending on the physics of the problem. The physical problem under consideration here is the expulsion of a jet of fluid from a nozzle containing a scalar quantity into an ambient fluid of the same static properties as the fluid being expulsed from the nozzle. As the fluid under consideration here is a gas at a high Mach number, the flow is compressible. Hence the following set of equations form the governing equations for the flow.

2.1.1 State variables

The flow can be described completely by the variables, density, ρ, the velocity vector $\boldsymbol{u}$ and the temperature, T, for a Newtonian fluid. These variables form the basic variables and all the other fields can be determined with the help of these variables. The variables are a function of space and time, $\rho(\mathbf{x}, t)$, $\boldsymbol{u}(\mathbf{x}, t)$, $T(\mathbf{x}, t)$ and they evolve

in both the temporal and the spatial domains according to the governing equations. The choice of these state variables though, is not unique. For example, in this thesis, instead of temperature, energy has been taken as a state variable and the temperature, T is expressed in terms of total energy, E.

2.1.2 Reynolds transport theorem

The Reynolds transport theorem[22] gives the general governing equation for the transport of a quantity based on the control volume approach. It can be written as

$$\frac{d}{dt}\int_{\Omega_{CM}} \rho\phi \, d\Omega = \frac{d}{dt}\int_{\Omega_{CV}} \rho\phi \, d\Omega + \int_{S_{CV}} \rho\phi(\boldsymbol{v} - \boldsymbol{v}_b)\cdot \boldsymbol{n} \, dS \tag{2.1}$$

where ϕ is the quantity being transported. $\boldsymbol{v}$ is the fluid velocity and $\boldsymbol{v}_b$ is the velocity with which the surface of the control volume is moving. In this thesis, the conservation equations have been derived for a fixed control volume, therefore $\boldsymbol{v}_b = 0$ and the time derivative for the first term becomes a local derivative. The left hand side is generally obtained by a balance of the rate of change of the intensive property per unit mass across the control mass.

2.1.3 Conservation of Mass

The conservation of mass for a compressible flow can be derived from the Reynolds transport theorem [22] and it expresses the fact that mass cannot be created or destroyed in a given control volume. The integral form is given by:

$$\frac{\partial}{\partial t}\int_{\Omega} \rho \, d\Omega + \int_{S} \rho\boldsymbol{u}\cdot \boldsymbol{n} \, dS = \mathfrak{S} \tag{2.2}$$

where Ω is the control volume and S is the surface enclosing the control volume, and $\boldsymbol{n}$ is the unit normal perpendicular to the surface, S and oriented outwards. $\mathfrak{S}$ is the source term which captures the fluid entering the domain at the left boundary and is zero everywhere else. Without loss of generality, it can be taken to be zero and adjusted in the numerical implementation.

Using the Gauss divergence theorem and assuming smoothness, we can express it in the differential form:

$$\begin{aligned} &\frac{\partial \rho}{\partial t} + \nabla \cdot (\rho \boldsymbol{u}) = 0 \\ &\frac{\partial \rho}{\partial t} + \frac{\partial}{\partial x_j}(\rho u_j) = 0 \end{aligned} \tag{2.3}$$

For appropriate solution of the equation, proper boundary conditions need to be imposed which are explained in section 3.4.

2.1.4 Conservation of Momentum

The momentum equations or the Navier–Stokes equations are the equations that govern the behaviour of momentum and can be again derived from the Reynolds transport theorem or from Newton's second law by balancing all forces acting on a control volume. The integral form is given by:

$$\frac{\partial}{\partial t}\int_{\Omega} \rho \boldsymbol{u}\, d\Omega + \int_{S} \rho \boldsymbol{u}\boldsymbol{u} \cdot \boldsymbol{n}\, dS = \sum \boldsymbol{f} \tag{2.4}$$

where Ω is the control volume and S is the surface enclosing the control volume, and $\boldsymbol{n}$ is the unit normal perpendicular to the surface, S and oriented outwards. $\boldsymbol{f}$ is the general expression of forces acting on the control volume. They can be classified in general into surface forces and body forces. For the problem under consideration, no body forces are assumed. The surface forces due to pressure and shear can be expressed in the form of the state variables by assuming that the fluid is Newtonian. Then the total stress tensor, τ_{tot} which is the molecular rate of transport of momentum can be expressed as:

$$\tau_{tot} = -\Big(p + \frac{2}{3}\mu \nabla \cdot \boldsymbol{u}\Big)\mathbf{I} + 2\mu \mathbf{D} \tag{2.5}$$

where μ is the dynamic viscosity, $\mathbf{I}$ is the identity tensor, p is the static pressure and $\mathbf{D}$ is the deformation tensor and is given by

$$\mathbf{D} = \frac{1}{2}\{\nabla \boldsymbol{u} + (\nabla \boldsymbol{u})^T\} \tag{2.6}$$

In Einstein summation convention, the stress tensor and the deformation can be expressed as

$$\begin{aligned} \tau_{tot} &= 2\mu D_{ij} - \Big(p + \frac{2}{3}\mu\frac{\partial u_j}{\partial x_j}\Big)\delta_{ij} \\ D_{ij} &= \frac{1}{2}\Big(\frac{\partial u_i}{\partial x_j} + \frac{\partial u_j}{\partial x_i}\Big) \end{aligned} \tag{2.7}$$

where δ_{ij} is the Kronecker delta ($\delta_{ij} = 1$, if $i = j$ and 0 otherwise). The dynamic viscosity is in general not constant and here for simplicity a dependence on the temperature is assumed and it is given by the Sutherland relation [23].

$$\frac{\mu}{\mu_\infty} = \Big(\frac{T}{T_\infty}\Big)^{3/2}\frac{1.4T_\infty}{T + 0.4T_\infty} \tag{2.8}$$

where μ_∞ and T_∞ are the ambient values.

Therefore using the Gauss divergence theorem again for Equation 2.4, we can obtain the differential form of the Navier–Stokes equations as

$$\frac{\partial(\rho \boldsymbol{u})}{\partial t} + \nabla \cdot (\rho \boldsymbol{u}\boldsymbol{u}) = \nabla \cdot \tau_{tot} \tag{2.9}$$

with appropriate boundary conditions as explained in section 3.4. To simplify notation we split the total stress tensor τ_{tot} into the deviatoric and the hydrostatic parts and therefore the final form of the Navier–Stokes equations can be written as

$$\frac{\partial \rho u_i}{\partial t} + \frac{\partial}{\partial x_j}(\rho u_i u_j + p\delta_{ij}) = \frac{\partial \tau_{ij}}{\partial x_j} \tag{2.10}$$

where τ_{ij} is the deviatoric stress tensor, $\tau_{ij} = \tau_{tot} + p\delta_{ij}$

2.1.5 Conservation of Energy

An equation for the conservation of energy is required to close the system of equations in a compressible flow along with an equation of state. Energy is a scalar and hence its governing equation forms a scalar transport equation and its transport is governed by the convective and the diffusive fluxes. The diffusive flux is described by a gradient approximation. Again the Reynolds transport theorem can be used to derive the energy equation. The energy, E here is the total energy and is composed of the internal energy and the kinetic energy.

$$\frac{\partial}{\partial t}\int_{\Omega} E\, d\Omega + \int_{S} E\boldsymbol{u}\cdot\boldsymbol{n}\, dS = \int_{S} k\nabla T\cdot\boldsymbol{n}\, dS + \int_{\Omega}(\boldsymbol{u}\cdot\nabla p + \tau_{tot} : \nabla\boldsymbol{u})\, d\Omega \quad (2.11)$$

where ":" denotes the tensor product operator, E is the total energy and is the sum of internal energy, $e = \rho c_v T$ and kinetic energy, $K = \rho u_i u_i/2$ that is $E = e + K$. κ denotes the thermal conductivity given by $\kappa = \mu c_p/Pr$. c_p is the specific heat at constant pressure and Pr is the Prandtl number which denotes the ratio of the momentum to the thermal diffusivity. c_p is given based on the properties of the gas.

Again, using the Gauss divergence theorem, we can get the differential form of the energy equation.

$$\frac{\partial E}{\partial t} + \frac{\partial}{\partial x_j}u_j(p+E) = \frac{\partial}{\partial x_j}\kappa\frac{\partial T}{\partial x_j} + \frac{\partial u_i\tau_{ij}}{\partial x_j} \quad (2.12)$$

with appropriate boundary conditions as explained in section 3.4.

The equation of state for an ideal gas gives the relation between the thermodynamic quantities, ρ, p and T as

$$p = \rho RT \quad (2.13)$$

where R is the gas constant. Subsequently, the speed of sound is given by, $U_{sound} = \sqrt{\gamma RT}$, where γ is the ratio of specific heats, $\gamma = c_p/c_v$.

2.1.6 Equation for scalar transport

In general it is possible to have two types of scalar transport, active scalar transport and passive scalar transport. Active scalars are those chemical species that affect the flow usually by reacting with each other such as oxygen and fuel in combustion and usually have a enthalpy production associated with them. Passive scalars on the other hand are passive and do not affect the flow, for example, a passive tracer added to a flow or a non-reacting gas in a flow.

Diffusion and convection are the two main aspects that govern the transport of the scalar in a flow. The convective transport is governed by the velocity of the flow and

the diffusive transport is governed by the diffusion coefficient of the scalar which is a property of the scalar.

Again as before, the governing equation can be derived from the Reynolds transport theorem. The integral form can therefore be written as

$$\frac{\partial}{\partial t}\int_{\Omega}\rho Y_k\, d\Omega + \int_{S}\rho Y_k \boldsymbol{u}\cdot\boldsymbol{n}\, dS = \int_{S}\boldsymbol{j}_k\cdot\boldsymbol{n}\, dS + \int_{\Omega}\omega_k\, d\Omega \tag{2.14}$$

where Y_k is the concentration of the kth chemical species where $k \in \{1, 2, ..., n\}$ and ω_k is the chemical source term which can form the source or sink for the kth chemical species $\boldsymbol{j}_k$ is the diffusive flux which is approximated by a binary flux approximation [24–26]. One has to be careful when using multi-component species as, with a binary flux approximation, the mass conservation for the all species may not be satisfied and a different flux approximation may have to be used. But for the purposes of this thesis, a binary flux approximation will be used and is given by $\boldsymbol{j}_k = \rho\kappa_{scal}\nabla Y_k$. Using this we get,

$$\frac{\partial}{\partial t}\int_{\Omega}\rho Y_k\, d\Omega + \int_{S}\rho Y_k \boldsymbol{u}\cdot\boldsymbol{n}\, dS = \int_{S}\rho\kappa_{scal}\nabla Y_k\cdot\boldsymbol{n}\, dS + \int_{\Omega}\omega_k\, d\Omega \tag{2.15}$$

Again using the Gauss divergence theorem, we can write the differential form as

$$\frac{\partial \rho Y_k}{\partial t} + \frac{\partial \rho u_j Y_k}{\partial x_j} = \frac{\partial}{\partial x_j}\left(\rho\kappa_{scal}\frac{\partial Y_k}{\partial x_j}\right) + \omega_k \tag{2.16}$$

with appropriate boundary conditions as explained in section 3.4.

2.1.7 Non-dimensionalization

A dimensionless form is usually advantageous when comparing results with experiments and with other computations and hence a non-dimensional form of the equations has been used in all the equations above. The variables have been made non-dimensional by using the ambient speed of sound, $U_{sound,\infty}$ as the reference velocity, the ambient density, ρ_∞ as the reference density, $\rho_\infty U^2_{sound,\infty}$ as the reference pressure and $U^2_{sound,\infty}/c_p$ as the reference temperature and the nozzle diameter, d_{jet} as the reference length. This type of non-dimensionalization is usually done in compressible flows because of the presence of sound waves. A second velocity scale that has been used is the jet exit velocity, U_{jet}. The non-dimensional constants that occur due to the scaling

are Reynolds number, Mach number, Prandtl number and Schmidt number and are defined as follows:

$$\begin{aligned} Re &= \frac{\rho_{jet} U_{jet} d_{jet}}{\mu_{jet}} \\ Ma &= \frac{U_{jet}}{c_{jet}} \\ Pr &= \frac{\mu c_p}{k} \\ Sc &= \frac{\mu}{\rho D_k} \end{aligned} \tag{2.17}$$

where k is the thermal conductivity of the fluid, D_k is the mass diffusivity of the species in the fluid, c_{jet} is the nozzle speed of sound.

2.2 Turbulence

The physical problem under consideration here is the compressible turbulent jet. It can be classified as a free turbulent flow as it is not a bounded flow and there are no physical walls present in the problem. As remarked upon before, the turbulent jet under consideration here is a jet of a fluid exiting a nozzle of diameter d_{jet} at a velocity U_{jet} into an ambient fluid of the same ambient properties as the jet shown in Figure 2.1. The initial flow close to the nozzle is laminar depending on the Reynolds number of the jet and is called the laminar core or the potential core of the flow. As the surrounding medium is a stationary fluid, a shear layer is formed across which there exists a change in the flow properties. This shear layer is unstable and disturbances grow that give the flow an instability that is similar to the Kelvin–Helmholtz instability which grows linearly. The laminar jet flow breaks down to turbulent flow downstream and there is a non-linear coupling between the different disturbances. In the downstream region the jet grows span-wise and height-wise and a phenomenon called entrainment occurs in which the jet incorporates the surrounding fluid. This is shown in Figure 2.1.

For sufficiently high Reynolds numbers, far downstream of the flow a similarity region is observed and a similarity solution can be obtained. Details about the similarity solutions and some more experimental and theoretical comparisons and results can be found in [2].

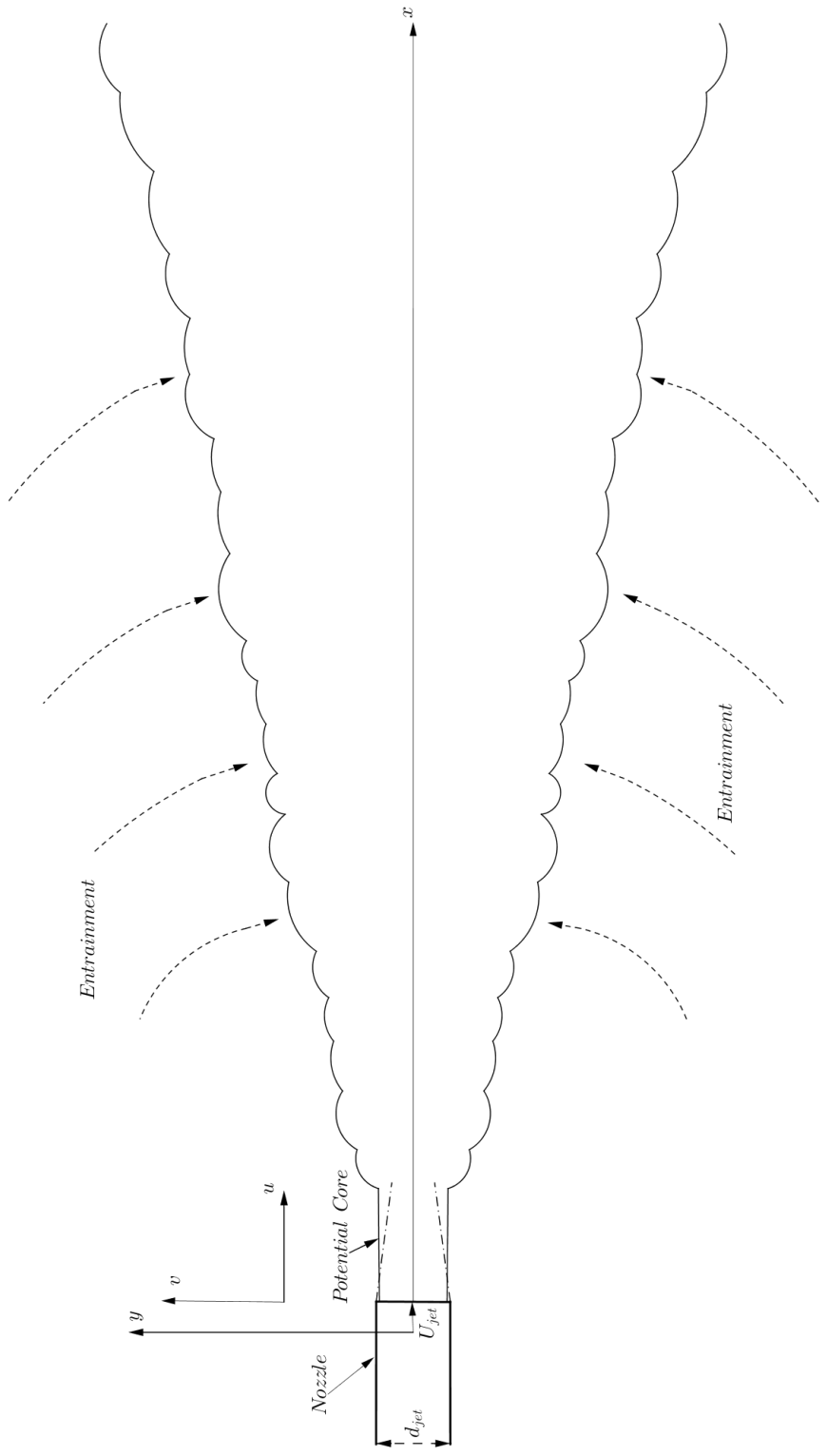

FIGURE 2.1: The free turbulent jet geometry

2.2.1 Effect of Reynolds number

The turbulent jet properties and the scales involved in the flow largely depend on the Reynolds number of the flow.

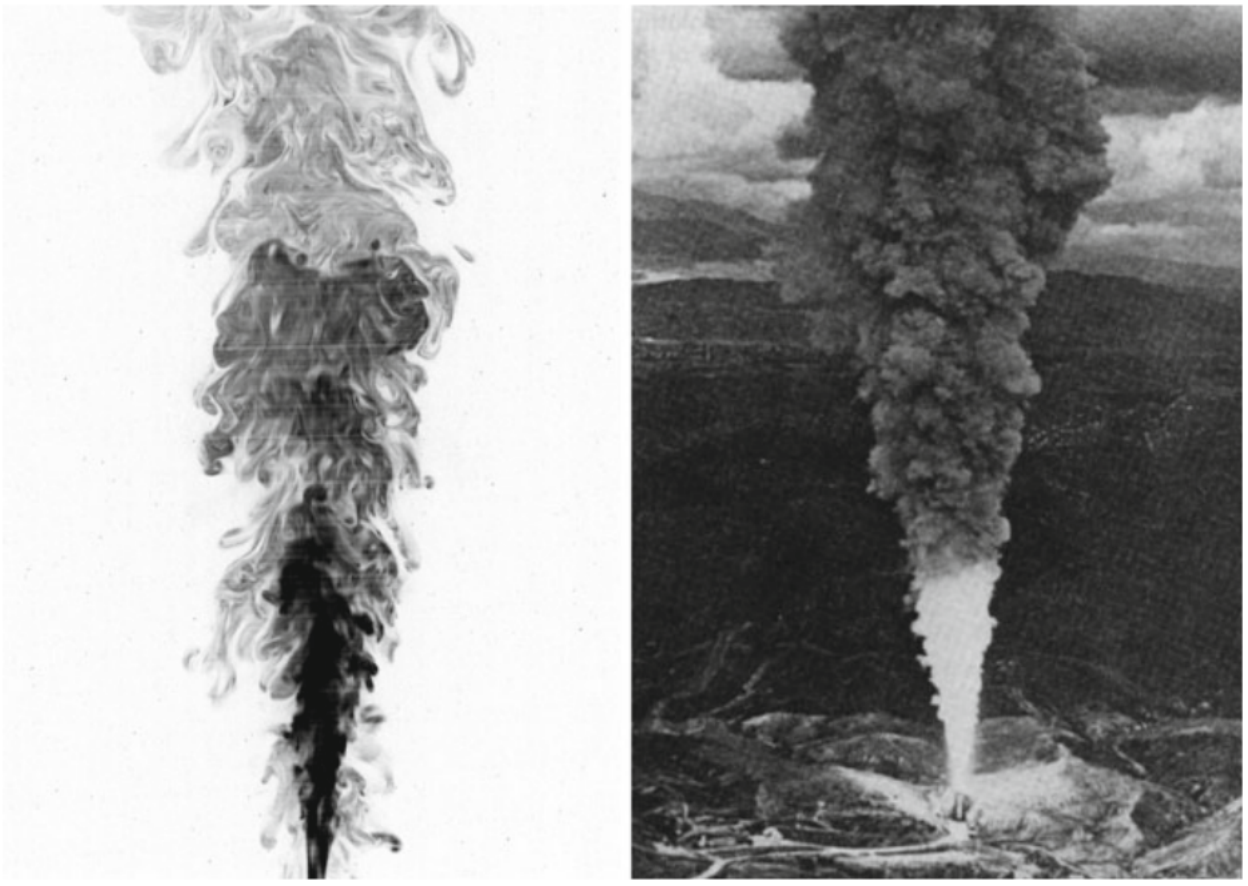

FIGURE 2.2: The effect of Reynolds number, Left: Re $= 2 \times 10^3$, Fukushima et.al [1] , Right: Re $= 2 \times 10^8$, TITAN IV rocket ground test exhaust plume. Taken from Nieuwstadt et.al [2]

As we can see from Figure 2.2 the rate of spreading of the jet is similar in both cases but the involved scales are largely different. At higher Reynolds numbers the Kolmogorov scale is much smaller because Re scales inversely to the Kolmogorov length scale, η. If the macroscopic length scale is given as $\mathcal{L}$, then

$$\frac{\mathcal{L}}{\eta} \sim Re^{3/4} \tag{2.18}$$

For example, for the problem that will be considered in this thesis, if the diameter of the nozzle is taken as the macroscopic length scale, $d_{jet} = 4 \times 10^{-3} m$, then the Kolmogorov scales for different Reynolds numbers are of the order as shown in Table

2.1. It can be easily seen that the range of scales for high Reynolds numbers is much larger than that for the low Reynolds numbers.

Kolmogorov scale rough estimation	
Reynolds Number, Re	*Kolmogorov Scale,* $\eta \times 10^{-3} m$
1500	0.017
3000	0.0098
8000	0.0047
15000	0.0029

TABLE 2.1: Kolmogorov scale estimation at different Reynolds numbers

2.2.2 Expected statistical behaviour

A number of experiments and computations have been performed on jet flow [1, 3–8, 27–30]. From the above experimental and computational results and also from theoretical derivations [2, 31] we can expect certain statistical behaviour in the flow properties as explained below.

1. A linear spreading rate has been observed in experiments and this behaviour is to be expected. This can be quantized by the jet half width or the jet radius as done in the experiments [1, 29, 32] or in numerical experiments [7, 33] or for simplified theoretical models as in [2].

2. A Gaussian type profile is expected for the axial velocity that decays along the axis [7, 32]. The axial velocity peaks along the axis of the jet and decays in directions perpendicular to the axes os the jet. This may also be inferred from the fact that the jet spreads in the downstream. A similar decay is expected in the radial velocity as well. The decay rates have been calculated in [7, 34].

2.3 Spatial discretization

Direct Numerical Simulation involves the solution of the governing Equations 2.3, 2.10, 2.12 and 2.16 by numerical methods and it involves the calculation of the solution without any turbulence modeling and without any models to account for the effect of small eddies as done in RANS simulations or LES but to directly capture these small scales themselves. Therefore the full governing equations are discretized in space and time.

2.3.1 Discretization techniques

In general the spatial discretizations can be classified into three types based on their approach to the physics of the problem, Finite Difference methods (FDM), Finite Volume Methods (FVM) and Finite Element Methods (FEM).

Finite Difference methods are the simplest of the methods and are very simple to implement and are based on direct discretization of the derivatives as in the governing equations. Finite Volume methods have a more physical approach are concerned with the fluxes across control volumes and this idea makes them suitable for conservation laws. Finite element methods are currently used lesser than its counterparts but hold promise for problems with complex and unstructured domains and have a very strong mathematical basis, hence stability and convergence proofs are available making the methods dependable and robust. The disadvantage of the Finite Element methods are that they are relatively more difficult to implement.

In this thesis, Finite Difference methods have been used because of their simplicity and ease of implementation.

2.3.2 Compact finite difference methods

Finite difference methods are the numerical methods that use the difference equations to approximate the differential equations. The most well known and basic finite differences include the Central difference method and the Upwind method. In central difference method, the stencil to calculate the i^{th} value uses the values of the functions to the left and right of i and gives them equal weights. The upwind scheme on the other hand uses values of the functions which are along the direction of the characteristic velocity giving them a higher weight. Therefore for the central schemes, the stencil is always symmetric whereas for the upwind it is skewed and weighted upwind of the characteristic velocity. For example, in the grid given in Figure 2.3, the central difference for the derivatives could be written as $f(i+2, i+1, i-1, i-2)$ for a fourth order method, whereas for an upwind method it would be $f(i, i-1, i-2)$ for a third order approximation when the characteristic velocity is towards the right.

In general, most finite difference methods based on difference equations require a large stencil to achieve a high order method. For example, a second order central difference method requires a 2 point stencil, but a 4th order central difference requires a 4 point stencil. Spectral methods are a class of methods that require a smaller stencil but the

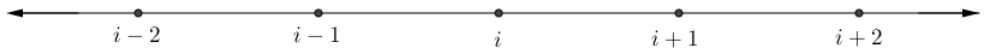

FIGURE 2.3: Discretization grid

class of problems to which they can be applied are restricted to simple domains and simple boundary conditions. Spectral methods also have the advantage that they have global dependence on the node values in their approximation. Compact finite difference methods are a class of methods that emulate this global dependence and hence can be said to have spectral like resolution as explained by Lele [35]. It was introduced by Hirsch [36] and Adam [37] but it has gained popularity quite recently, especially in the simulation of turbulent flows because of their ability to capture a wide range of scales while being applicable to general boundary conditions and relatively more general domains. In general they solve for the derivatives by using an approximation of the form

$$\begin{aligned} \beta f'_{i-2} + \alpha f'_{i-1} + \alpha f'_i + \alpha f'_{i+1} + \beta f'_{i+2} = c\frac{f_{i+3} - f_{i-3}}{6h} \\ +b\frac{f_{i+2} - f_{i-2}}{4h} \\ +a\frac{f_{i+1} - f_{i-1}}{2h} \end{aligned} \tag{2.19}$$

where f' is the first derivative of the function f, h is the step size and the coefficients α, β, a, b, c are calculated by matching the Taylor series expansions of the required order. In general, more function values can always be used to approximate the derivative. Different orders are obtained when Taylor series expansions of different orders are matched and can be referred to from [35].

Using the general form in Equation 2.19, we can obtain a formal highest order of accuracy of 10. This would result in a penta-diagonal scheme, schemes that require solution of a penta-diagonal matrix linear equation to obtain the derivatives. In general, it is easier to solve for a tri-diagonal system because it can be solved very efficiently by the Thomas algorithm. Therefore it is usually more efficient to increase the stencil width and solve for a tri-diagonal system than the other way. To solve for the derivatives, linear systems of the form given in Equation 2.20 need to be solved.

$$A\mathbf{f}' = B\mathbf{f} \tag{2.20}$$

where A is the matrix containing the coefficients of the left hand side of Equation 2.19 and B contains the right hand side coefficients. $\mathbf{f}$ is the right hand side vector that contains the values of the function at the required node values and $\mathbf{f}'$ values of the unknown derivatives at the required node points. The solution of the matrix equation 2.20 requires the inversion of the matrix A to solve for the unknown vector $\mathbf{f}'$.

Mahesh [38] proposed schemes that which are a variation of the schemes of Lele in that he calculated both the first and second derivative simultaneously. Boersma [7, 33] proposed a staggered formulation to calculate the derivatives of the governing equations thereby removing some of the stability issues due to aliasing errors faced by Lele [35]. The staggered formulation has been used in this thesis and has been explained in the next section.

2.3.3 Staggered and Co-located grids

A grid can be classified into two categories. Staggered formulation and co-located formulation. This has been shown in the Figure 2.4. In a staggered grid, the fields exist at the cell faces as well as the cell nodes. The scalar fields such as density (ρ), concentration(Y_k), pressure(p), temperature(T) and energy(E) exist at the cell nodes where as the vector fields exist at the cell faces. This has been illustrated in Figure 2.4(a). In a co-located grid, all the fields, the scalar and the vector exist on the cell node values only and has been illustrated in Figure 2.4(b). For simplicity, only a 2D grid has been shown but the same idea extends to 3D but the cell faces lie on the actual faces of the cube of the 3D grids.

Both the types of grids have their advantages and dis-advantages. A co-located grid is easily extended to curvilinear grid and does not involve any interpolations to calculate the node values but it may suffer from stability issues. The staggered grid on the other hand is more stable and robust but involves more work due to interpolations to and from the node values and is also not easily adapted to complex grids. In this thesis, a staggered grid has been used to because the grid is relatively simple and stability is of more importance.

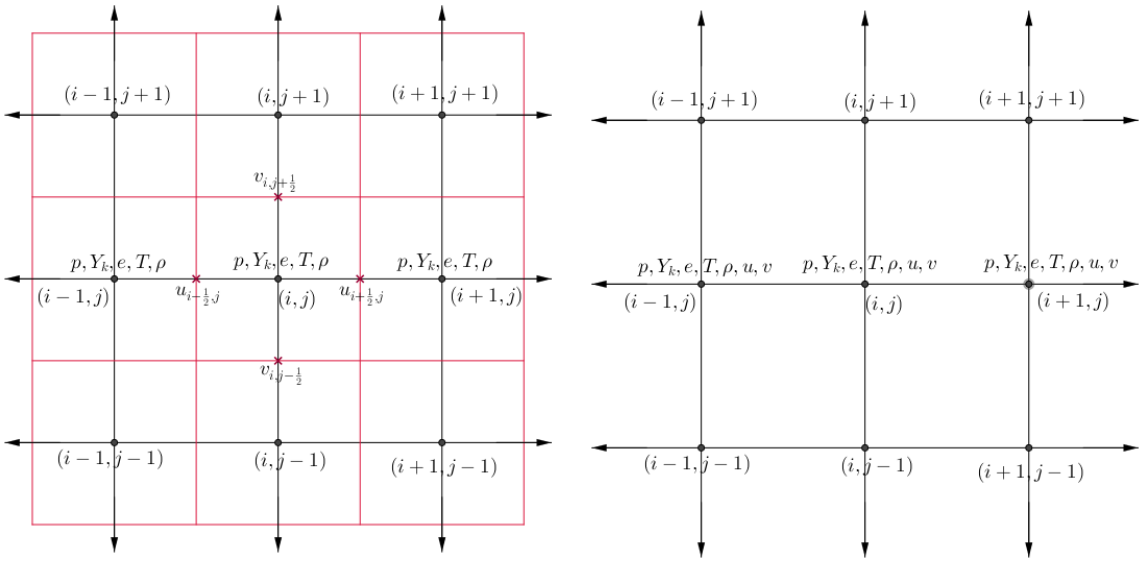

(a) Staggered discretization grid

(b) Co-located discretization grid

FIGURE 2.4: 2D grid for discretization

2.3.4 Staggered Compact schemes

Boersma [4] proposed staggered compact finite difference schemes of very high order (upto 10th and 12th), a variation of the schemes proposed by Lele [35]. For simulation of a high Reynolds number jet, it is essential to discretize with a high order method to allow for accurate solution while keeping the spatial step relatively large. The schemes were of the form

$$\begin{aligned}\alpha f'_{i-1} + f'_i + \alpha f'_{i+1} = d\frac{f_{i+7/2} - f_{i-7/2}}{h} + c\frac{f_{i+5/2} - f_{i-5/2}}{h} \\ +b\frac{f_{i+3/2} - f_{i-3/2}}{h} + a\frac{f_{i+1/2} - f_{i-1/2}}{h}\end{aligned} \tag{2.21}$$

where f' is the first derivative of the function f, h is the spatial step size and the coefficients α, a, b, c, d are calculated by matching the Taylor series expansions as before. The coefficients that were used for the 10th or order method are given in Appendix B.

It can be seen that near the boundaries, a large stencil is not available. There are two choices available. One would be to reduce the order uniformly near the boundaries and use a one sided scheme at the boundaries. The other would be the creation of ghost points and the values at the ghost points are obtained by appropriate order extrapolations. In this thesis, the the order of the schemes are reduced uniformly near the boundaries as explained in [4].

2.3.5 Calculating derivatives

It can be seen from the governing Equations 2.3–2.16 that we need to calculate the first derivative and the second derivative. We calculate the second derivative by taking the first derivative as the right hand side function and not through an explicit formula. When the governing equations are cast in a non-conservative form, it becomes necessary to have a rule for the explicit calculation of the second derivative. This is sometimes necessary to dampen the high wave number components that cause instability but the staggered scheme does not require this [4]. It can also be observed that many of the terms involve the product of a scalar and a vector field and their subsequent derivatives. Therefore, an interpolation rule has to be used to calculate the vector field values at the cell nodes and the scalar field values at the cell faces. A appropriate high order method has to be used to interpolate so that the overall order of the calculation of the derivative does not reduce. A similar compact interpolation rule as in Equation 2.21 has been used.

$$\begin{aligned} \alpha f_{i-1} + f_i + \alpha f_{i+1} = d(f_{i+7/2} + f_{i-7/2}) + c(f_{i+5/2} + f_{i-5/2}) \\ + b(f_{i+3/2} + f_{i-3/2}) + a(f_{i+1/2} + f_{i-1/2}) \end{aligned} \tag{2.22}$$

where f is the function to be interpolated from the cell node values to the cell faces and the coefficients α, a, b, c, d are calculated by matching the Taylor series expansions as before.

For example, if the term $\frac{\partial \rho u_i u_j}{\partial x_j}$ has to be calculated, then first the velocities are interpolated to the cell nodes using the interpolation rule in 2.22 and the product is formed at the cell nodes. The derivatives are then calculated using only the cell node values using the rule 2.21. If an interpolation from the cell faces to the cell node is required, then the interpolation rule is shifted by half a cell and the same rule is used again.

It has to be noted that the derivative and the interpolation rules, 2.21,2.22 are valid only for uniform grids. To extend it to non-uniform grids, a mapping is done to transform the non-uniform grid to a uniform grid and the derivatives are calculated on the uniform grid.

$$\begin{aligned} \frac{\partial f}{\partial x} &= \frac{\partial f}{\partial X}\frac{\partial X}{\partial x} \\ \frac{\partial f}{\partial X} &= \frac{\partial f}{\partial x}\left(\frac{\partial X}{\partial x}\right)^{-1} \end{aligned} \tag{2.23}$$

where x is the coordinate on the non-uniform grid and X is the coordinate on the uniform grid.

A known function, which has the property that its derivative with respect to the non-uniform grid coordinate it does not go to zero inside the computational domain is used to is used to calculate $\frac{\partial X}{\partial x}$.

But this mapping cannot be used for the function values itself. As stated in [4] and shown in [39], a mapping could be constructed for the non-uniform grids but this does not conserve the kinetic energy numerically which is usually essential for a stable numerical scheme. Therefore the same interpolation rule 2.22 is used on the non-linear grid. This reduces the formal order of accuracy but conserves kinetic energy numerically.

2.3.6 Drawbacks

When the compact finite difference methods are used to discretize the scalar transport equations, oscillations are observed in the regions of discontinuities. This can make the values of the field unphysical for example, the concentration of a scalar can become negative, which is physically not possible.

The reason for this can be understood by observing that the schemes are central therefore the information is taken from both the upwind side and the downwind side of the point in consideration with equal weights. This is suitable for smooth regions but for regions of discontinuities, the characteristics converge and therefore the information taken from the downwind will cause oscillations and eventual instability. Therefore for such regions upwind stencils must be used to obtain the non-oscillatory behaviour.

Therefore for the scalar transport equations, it is essential to use methods that are non-oscillatory such as ENO [10] or WENO [40] that can switch to upwind schemes near the discontinuities to accurately model the physics. The idea of these schemes are explained in the next sections.

2.3.7 Essentially non-oscillatory schemes

Essentially non-oscillatory (ENO) schemes have the property that they make sure that the solution is non-oscillatory especially near the discontinuities. As explained earlier, this is required for problems in which one might expect solution to be oscillatory. ENO

schemes were first introduced by Harten et.al [10] and were worked on extensively by Shu and Osher [12].

The main property that these schemes satisfy is that their Total Variation is either diminishing or bounded, that is they are TVD or TVB. Total variation is defined as

$$TV(u) = \sum_j |u_{j+1} - u_j| \tag{2.24}$$

A scheme is said to be Total Variation Diminishing (TVD) if $TV(u^{n+1}) \leq TV(u^n)$ and Total Variation Bounded (TVB) if $TV(u^n) \leq B$ in $0 \leq t \leq T$, where B is some fixed value only based on $TV(u^0)$ for all time steps and time step sizes. Though this can be shown numerically, a theoretical proof for the TVB-ness cannot be easily shown.

The main idea of ENO schemes is to use multiple candidate stencils and select the stencil that is the smoothest in some sense. There are many measures of smoothness available but the simplest one is through a Newton's divided difference. If $v(x)$ is the function which has to be solved for, then a primitive function $Q(x)$ of $v(x)$, which is a measure of the function in the cell is given in terms of the function by

$$Q(x_{i+\frac{1}{2}}) \equiv \sum_{j=-\infty}^{i} \int_{x-\frac{1}{2}}^{x+\frac{1}{2}} v(\zeta) d\zeta = \sum_{j=-\infty}^{i} \overline{v}_j \Delta x_j \tag{2.25}$$

If for instance $Q(x)$ is the function whose smoothness has to be determined in the stencils, then we consider the value of the j-th order divided difference when $j \geq 1$ as

$$\begin{aligned} Q[x_{i-\frac{1}{2}}, ..., x_{i+j-\frac{1}{2}}] &\equiv \frac{Q[x_{i+\frac{1}{2}}, ..., x_{i+j-\frac{1}{2}}] - Q[x_{i-\frac{1}{2}}, ..., x_{i+j-\frac{3}{2}}]}{x_{i+j-\frac{1}{2}} - x_{i-\frac{1}{2}}} \\ Q[x_{i-\frac{1}{2}}] &\equiv Q(x_{i-\frac{1}{2}}) \end{aligned} \tag{2.26}$$

A k-th degree interpolation polynomial can be formed using the divided differences that interpolates $Q(x)$ using $k+1$ points.

$$I_1(x) = \sum_{j=0}^{k} Q[x_{i-r-\frac{1}{2}}, ..., x_{i-r+j-\frac{1}{2}}] \prod_{m=0}^{j-1} \left(x - x_{i-r+m-\frac{1}{2}} \right) \tag{2.27}$$

Taking its derivative, we can directly obtain the interpolation function for the function, $v(x)$.

$$I_2(x) = \sum_{j=1}^{k} Q[x_{i-r-\frac{1}{2}}, ..., x_{i-r+j-\frac{1}{2}}] \sum_{m=0}^{j-1} \prod_{\substack{l=0 \\ l \neq m}}^{j-1} \left(x - x_{i-r+l-\frac{1}{2}} \right) \tag{2.28}$$

These interpolation polynomials will be used later.

Now, for divided differences we know that

$$Q[x_{i-\frac{1}{2}}, ..., x_{i+j-\frac{1}{2}}] = \frac{Q^{(j)}(\zeta)}{j!} \tag{2.29}$$

for $x_{i-\frac{1}{2}} < \zeta < x_{i+j-\frac{1}{2}}$, if the function $Q(x)$ is smooth inside the stencil. Otherwise, if $Q(x)$ is discontinuous at some point inside the stencil, then

$$Q[x_{i-\frac{1}{2}}, ..., x_{i+j-\frac{1}{2}}] = \mathcal{O}\left(\frac{1}{\Delta x^j} \right) \tag{2.30}$$

Therefore starting with a stencil of S = $\{x_{i-\frac{1}{2}}, x_{i+\frac{1}{2}}\}$, points are added successively to the stencil until a discontinuous stencil is encountered or until the maximum stencil width is reached. And this is the smoothest stencil that will avoid the Gibbs like phenomena in the solution. For detailed procedure, [41] can be referred to.

But there are some improvements possible in the ENO methods and these are performed in the WENO methods.

2.3.8 Weighted Essentially non-oscillatory methods

Weighted Essentially non-oscillatory (WENO) schemes were first introduced by Liu et.al [14] after realizing that certain improvements were possible in the ENO methods.

1. The selection of the smoothest was not robust and was affected by even round-off errors. Moreover, in the smooth regions as well there was a "free adaptation" of stencils which was not necessary and reduced the order of accuracy in certain situations.

2. The numerical flux calculated from the stencil will not be smooth as the stencil may change at neighbouring points.

3. In general k stencils were considered, covering $(2k-1)$ cells, but only one stencil that was smoothest was chosen, obtaining a k-th order accuracy. The idea of WENO, as will be seen below was to use all $(2k-1)$ cells in the stencils to formally get an accuracy of $(2k-1)$-th order in at least the smooth regions.

As the name suggests, WENO is the procedure of weighting all the stencils that span $(2k-1)$ cells and not selection of the smoothest stencil as in ENO. Therefore, the stencil that is the smoothest would be assigned the maximum weight and the stencil containing the discontinuities would be assigned no weight. This solves all the issues that were present in the ENO methods.

Consider the k candidate stencils

$$S_r(i) = \{x_{i-r}, ..., x_{i-r+k-1}\}, \qquad r = 0, ..., k-1 \tag{2.31}$$

to get k different reconstructions for the value $v_{i+\frac{1}{2}}$ from the average values in the cells,

$$v^{(r)}_{i+\frac{1}{2}} = \sum_{j=0}^{k-1} c_{rj}\overline{v}_{i-r+j}, \qquad r = 0, ..., k-1 \tag{2.32}$$

The idea of WENO is to use a convex combinations of all the $v^{(r)}_{i+\frac{1}{2}}$ defined in Equation 2.32 as an approximation to $v_{i+\frac{1}{2}}$,

$$v_{i+\frac{1}{2}} = \sum_{j=0}^{k-1} \omega_r v^{(r)}_{i+\frac{1}{2}} \tag{2.33}$$

The crux of the idea is the choosing of the coefficients ω_r. The required properties of the coefficients are:

1. For stability and consistency, it is required that

$$\omega_r \geq 0; \qquad \sum_{r=0}^{k-1} \omega_r = 1 \tag{2.34}$$

2. When the function $v(x)$ is smooth in all the stencils considered in Equation 2.31, we require that the order of the approximation be $2k-1$ and there exist coefficients d_r such that

$$v_{i+\frac{1}{2}} = \sum_{j=0}^{k-1} d_r v_{i+\frac{1}{2}}^{(r)} = v(x_{i+\frac{1}{2}}) + \mathcal{O}(\Delta x^{2k-1}) \tag{2.35}$$

we see that d_r satisfies the consistency and stability properties in enumeration 1. Therefore, in the smooth case we would like to have

$$\omega_r = d_r + \mathcal{O}(\Delta x^{k-1}) \qquad\qquad r = 0, ..., k-1 \tag{2.36}$$

which would give a $(2k-1)$-th order accuracy because,

$$\begin{aligned} \sum_{j=0}^{k-1} \omega_r v_{i+\frac{1}{2}}^{(r)} - \sum_{j=0}^{k-1} d_r v_{i+\frac{1}{2}}^{(r)} &= \sum_{j=0}^{k-1} (\omega_r - d_r)(v_{i+\frac{1}{2}}^{(r)} - v(x_{i+\frac{1}{2}})) \\ &= \sum_{j=0}^{k-1} \mathcal{O}(\Delta x^{k-1}) \mathcal{O}(\Delta x^{k}) = \mathcal{O}(\Delta x^{2k-1}) \end{aligned} \tag{2.37}$$

$$v_{i+\frac{1}{2}} = \sum_{j=0}^{k-1} \omega_r v_{i+\frac{1}{2}}^{(r)} = v(x_{i+\frac{1}{2}}) + \mathcal{O}(\Delta x^{2k-1}) \tag{2.38}$$

3. If any of the stencils has a discontinuity, then we would like those stencils to be assigned a weight of 0 to obtain the ENO behaviour.

4. The weights should be a smooth function of the cell averages of the function. The weights described here are taken from [41] and [15] and are C^∞, infinitely continuous differentiable.

5. Also, it is preferred to have coefficients that are computationally efficient, thus, polynomials are preferred over exponential type functions.

Keeping all the above things in mind, we can arrive at the following form for the weights

$$\omega_r = \frac{\alpha_r}{\sum_{s=0}^{k-1} \alpha_s}, \qquad\qquad r = 0, ..., k-1 \tag{2.39}$$

with

$$\alpha_r = \frac{d_r}{(\epsilon + \beta_r)^2} \tag{2.40}$$

where ϵ is a small positive number used to prevent the denominator from going to zero. β_r are called the "smoothness indicators" and are used to calculate the smoothness of the function $v(x)$ in the stencil $S_r(i)$. The calculation of α_r shown above is one way to calculate the coefficients but there exist many other improved ways which will be explained later. Therefore, if the function is smooth in the stencil $S_r(i)$, then $\beta_r = \mathcal{O}(\Delta x^2)$ and if it has a discontinuity then $\beta_r = \mathcal{O}(1)$. Therefore, for smooth stencils, $\omega_r = \mathcal{O}(1)$ and for stencils with discontinuities, $\omega_r = \mathcal{O}(\Delta x^4)$.

A reconstruction polynomial of order $(k-1)$-th degree can be constructed with the stencil $S_r(i)$ to approximate the value $v(x_{i+\frac{1}{2}})$. The total variation is a good measurement of smoothness [40, 41]. Therefore, it is logical to minimize the total variation for this reconstruction polynomial inside the stencil. Therefore, considering the reconstruction polynomial as $p_r(x)$ for the stencil $S_r(i)$, Shu [15] derived the following function for the smoothness indicator β_r,

$$\beta_r = \sum_{l=1}^{k-1} \int_{x_{i-\frac{1}{2}}}^{x_{i+\frac{1}{2}}} \Delta x^{2l-1} \left(\frac{\partial^l p_r(x)}{\partial^l x} \right)^2 dx \tag{2.41}$$

We observe that the right hand side is just a sum of the squared of the scaled $\mathcal{L}^2$ norms for all derivatives of the interpolation polynomial $p_r(x)$. It has been shown in [15] that the accuracy condition is satisfied, even near the smooth extrema and that the smoothness measurement is smoother than the divided difference measurement based on the $\mathcal{L}^1$ norm [41].

2.3.9 Combining WENO and compact finite difference methods

Ideally we would like to obtain a scheme that can capture a wide range of scales, not be dissipative and be able to capture discontinuities accurately. But practically this is not achievable because schemes that have to capture discontinuities are dissipative. To obtain the best of both worlds, compact schemes were designed by [21] which used a hybrid of both upwind and central schemes and used a non-linear weighting procedure to assign weights taking into account the smoothness of the stencils similar to the WENO procedure.

The WENO idea in [41], was to interpolate the value of the function f at the cell center, $x_{i+\frac{1}{2}}$ by a $(2r-1)$ order approximation by

$$\tilde{f}_{i+\frac{1}{2}} = g^{2r-1}(f_{i-r+1}, ..., f_{i+r-1}) \tag{2.42}$$

The WENO idea was to split the stencil S^{2r-1} into r sub-stencils from $k = 0, ..., (2r-1)$ as

$$S_k^{2r-1} = (x_{i+k-r+1}, ..., x_{i+k}) \tag{2.43}$$

and using the r-th order approximation from each of the stencils,

$$\tilde{f}^k_{i+\frac{1}{2}} = g^r_k(f_{i+k-r+1}, ..., f_{i+k}) \tag{2.44}$$

where

$$g^r_k(w_0, ..., w_{r-1}) = \sum_{j=0}^{r-1} a^r_{kj} w_j \tag{2.45}$$

to form a convex combination of the interpolations above to get

$$\tilde{f}_{i+\frac{1}{2}} = \sum_{k=0}^{r-1} \omega^r_k g^r_k(f_{i+k-r+1}, ..., f_{i+k}) \tag{2.46}$$

where ω^r_k is the non-linear weight obtained as before from Equations 2.39-2.41.

To combine with the compact finite difference method, we just substitute the interpolated values to the Equation 2.21 to get the derivative of the required function.

2.3.10 Hybrid weighted non-linear interpolation

As discussed before, central schemes have very low dissipation and upwind schemes have a lot dissipation. Dissipation is required to capture discontinuities and hence the WENO scheme uses the upwind stencil to accurately model the discontinuities. An idea proposed by Liu et al [21] proposes a hybrid weighted non-linear interpolation that incorporates the idea of WENO to assign weights to a hybrid scheme consisting of upwind and central stencils as explained below for a 6th order interpolation.

The sixth order central stencil is given by

$$\tilde{f}^{cent}_{i+\frac{1}{2}} = \frac{1}{256}(3f_{i-2} - 25f_{i-1} + 150f_i + 150f_{i+1} - 25f_{i+2} + 3f_{i+3}) \tag{2.47}$$

and the 5th order upwind stencil is given by

$$\tilde{f}^{upw}_{i+\frac{1}{2}} = \frac{1}{128}(3f_{i-2} - 20f_{i-1} + 90f_i + 60f_{i+1} - 5f_{i+2}) \tag{2.48}$$

The stencil is given by $S = \{x_{i-2}, ..., x_{i+3}\}$. Four third order interpolations can be formed from the sub-stencils as

$$\begin{aligned}
\tilde{f}^{0}_{i+\frac{1}{2}} &= \frac{1}{8}(3f_{i-2} - 10f_{i-1} + 15f_i) \\
\tilde{f}^{1}_{i+\frac{1}{2}} &= \frac{1}{8}(-f_{i-1} + 6f_i + 3f_{i+1}) \\
\tilde{f}^{2}_{i+\frac{1}{2}} &= \frac{1}{8}(3f_i + 6f_{i+1} - f_{i+2}) \\
\tilde{f}^{3}_{i+\frac{1}{2}} &= \frac{1}{8}(15f_{i+1} - 10f_{i+2} + 3f_{i+3})
\end{aligned} \tag{2.49}$$

A hybrid linear interpolation can be written as

$$\tilde{f}^{hyb}_{i+\frac{1}{2}} = (1-\sigma)\tilde{f}^{upw}_{i+\frac{1}{2}} + \sigma\tilde{f}^{cent}_{i+\frac{1}{2}} = \sum_{j=0}^{3} y_j \tilde{f}^{j}_{i+\frac{1}{2}} \tag{2.50}$$

where y_j are the linear weights and σ is the parameter that controls the contribution of the upwind and the central stencil and $0 \leq \sigma \leq 1$. As seen, if $\sigma = 1$, then it is a fully central scheme and if $\sigma = 0$, then it is a upwind scheme with no central contribution. For the definition of σ we use the ideas from Ren et. al. [19]. He suggests a σ to be defined as a continuous function rather than a abrupt function as done by Pirozzoli [42] and defines it as

$$\sigma = min\left(1, \frac{\varrho_{i+\frac{1}{2}}}{\varrho_c}\right) \tag{2.51}$$

where ϱ_c is a parameter that controls the dissipation and $\varrho_{i+\frac{1}{2}}$ is a smoothness indicator defined by $\varrho_{i+\frac{1}{2}} = min(\varrho_{i-1}, \varrho_i, \varrho_{i+1}, \varrho_{i+2})$ and ϱ_i has been defined by

$$\varrho_i = \frac{|2(f_{i+1} - f_i)(f_i - f_{i-1})| + \delta}{(f_{i+1} - f_i)^2 + (f_i - f_{i-1})^2 + \delta} \tag{2.52}$$

where δ is another parameter that gains importance for DNS of turbulent, viscous flows, because of the turbulent fluctuations which may make the smoothness indicator very small making the scheme very dissipative when WENO is used. Hence to reduce the dissipation and make sure that the turbulent fluctuations are not damped, Ren[19] suggests to use δ as

$$\delta = \frac{0.9\varrho_c}{1 - 0.9\varrho_c}\xi^2 \tag{2.53}$$

and ξ is a parameter that controls the dissipation and it has been verified that when $max((f_i - f_{i-1}), (f_{i+1} - f_i), (f_{i+2} - f_{i+1})) \leq \xi$, we get $\sigma \geq 0.9$, therefore making the central sub-scheme dominate the hybrid scheme. The value of ξ serves as a threshold value and turbulent fluctuations lesser than ξ will not be damped by the WENO scheme.

Writing it explicitly we obtain the final form.

$$\begin{aligned} \tilde{f}^{hyb,lin}_{i+\frac{1}{2}} = &\frac{3y_0}{8}f_{i-2} - \frac{10y_0 + y_1}{8}f_{i-1} \\ &+ \frac{15y_0 + 6y_1 + 3y_2}{8}f_i + \frac{3y_1 + 6y_2 + 15y_3}{8}f_{i+1} \\ &- \frac{y_2 + 10y_3}{8}f_{i+2} + \frac{3y_3}{8}f_{i+3} \end{aligned} \tag{2.54}$$

The linear weights are given by

$$y_0 = \frac{2 - \sigma}{32}, y_1 = \frac{5(4 - \sigma)}{32}, y_2 = \frac{5(2 + \sigma)}{32}, y_3 = \frac{\sigma}{32} \tag{2.55}$$

To get the WENO scheme, we replace the linear weights by the non-linear weights. Therefore, the hybrid non-linear interpolation is

$$\begin{aligned} \tilde{f}^{hyb}_{i+\frac{1}{2}} = &\frac{3\omega_0^M}{8}f_{i-2} - \frac{10\omega_0^M + \omega_1^M}{8}f_{i-1} \\ &+ \frac{15\omega_0^M + 6\omega_1^M + 3\omega_2^M}{8}f_i + \frac{3\omega_1^M + 6\omega_2^M + 15\omega_3^M}{8}f_{i+1} \\ &- \frac{\omega_2^M + 10\omega_3^M}{8}f_{i+2} + \frac{3\omega_3^M}{8}f_{i+3} \end{aligned} \tag{2.56}$$

where the weights ω_j^M are the non-linear WENO weights which have been mapped using a mapping function,

$$m_j(\omega) = \frac{\omega(y_j + y_j^2 - 3y_j\omega + \omega^2)}{y_j^2 + \omega(1 - 2y_j)} \tag{2.57}$$

This mapping function is required to maintain accuracy at smooth extrema as pointed out by [20]. This mapping function recovers the order of accuracy, ω_j to the linear weights y_j at the critical points. The properties of $m_j(\omega)$ are

1. It is a non-decreasing monotone function.
2. $0 \leq m_j(\omega) \leq 1, m_j(0) = 0$ and $m_j(1) = 1$
3. $m_j(y_j) = y_j, m_j'(y_j) = m_j''(y_j) = 0$

The mapped non-linear weights, ω_j^M can be calculated as

$$\omega_j^M = \frac{\alpha_j^M}{\sum_{d=0}^{3} \alpha_d^M}, \qquad \alpha_j^M = m_j(\omega_j), \qquad j = 0, ..., 3 \tag{2.58}$$

where the non-linear weights, ω_j are the WENO weights given by

$$\omega_j = \frac{\alpha_j}{\sum_{d=0}^{3} \alpha_d}, \qquad \alpha_j = y_j\left(C + \frac{\tau}{\epsilon + \beta_j}\right), \qquad j = 0, ..., 3 \tag{2.59}$$

where the α_j above is defined to include both the linear weights and the non-linear weights and hence is different from the usual WENO weights. C is a parameter that assigns a weight to the linear part of the weight. As observed by Hu [43], changing C changes the numerical dissipation only slightly. A larger C produces less numerical dissipation. Very large values of C produce numerical instabilities for flows with strong shocks. ϵ is a small positive number used to prevent the denominator from going to zero. τ is called the reference smoothness indicator defined by

$$\tau = \beta_3 - \frac{1}{8}(\beta_0 + 6\beta_1 + \beta_2) \tag{2.60}$$

and finally the smoothness indicators, β_j are as given in [21].

2.3.11 Flux splitting

When an upwind scheme is used, the characteristic velocity of the equation must be looked at carefully. Depending on whether the derivative of the flux is positive or negative, the scheme would be upwind or downwind and therefore the stencil must be adapted accordingly. All the above interpolations are given for a positive flux derivative. When the flux derivative is negative, the stencil is mirrored about the point $x_{i+\frac{1}{2}}$ in the above cases as shown in Figure 2.5. It is important to split the fluxes appropriately to make sure that the upwind stencil is only used on the positive fluxes and the downwind on the negative fluxes.

In general, it is possible to split the fluxes into positive and negative fluxes as

$$f(u) = f^{+}(u) + f^{-}(u) \tag{2.61}$$

where

$$\frac{df^{+}(u)}{du} \geq 0 \qquad \frac{df^{-}(u)}{du} \leq 0 \tag{2.62}$$

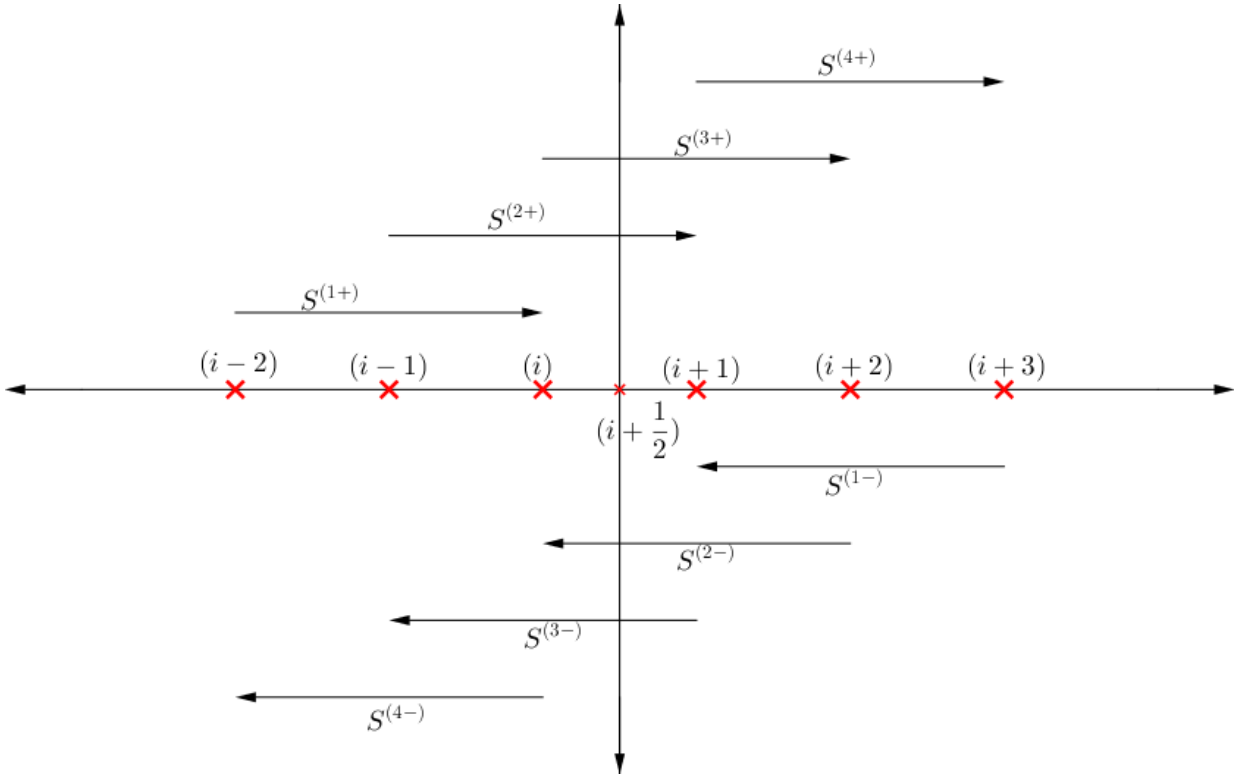

FIGURE 2.5: Stencils for flux splitting

The important aspect to note while splitting the fluxes is that we need to have the split fluxes to have as many derivative as the order of the scheme in the least. There are many choices for flux splitting methods.

We use the Lax-Friedrichs flux splitting, where the total flux is split as $f^{\pm}(u) = \frac{1}{2}(f(u) \pm \alpha u)$. There are two variants of the Lax-Friedrichs splitting, one is the global splitting and the other is the local splitting, the difference between the two being the value of $\alpha = \max(|f'(u)|)$, where the maximum is taken over either the global or the local range of u. For the advection equation, the $f'(u)$ is nothing but the Jacobian of the governing equation and is called its characteristic velocity. It is the slope of the characteristics of the solution when using the method of characteristics.

2.4 Temporal Discretization

Once the governing equations have been discretized in the spatial domain, they need to be stepped through time to evolve them in the temporal domain. Generally speaking, by discretizing the equations in the spatial domain and not in the temporal domain, we get a semi-discrete equation which has to be integrated in time to obtain the value of the unknown at each of the physical time steps.

2.4.1 Implicit and Explicit methods

Explicit methods are those methods that can calculate the next time steps from the information of the previous time steps only. Therefore, explicit methods do not have the need to solve linear systems to obtain the unknown values. In general explicit methods can be written by

$$U^{n+1} = F(t_k, U^k, \Delta t), \qquad t_k \in \{t_n, .., t_{n+1}\}, U^k \in \{U^m, m | m < n+1\} \tag{2.63}$$

Implicit methods on the other hand have a implicit dependence on the information which is not yet known. Therefore, they require a solution of a linear system to obtain the unknown value.

$$U^{n+1} = F(t_k, U^k, \Delta t), \quad t_k \in \{t_n, .., t_{n+1}\}, U^k \in \{U^m, m | m \leq n + l\} \;\; l \in \{1, 2, 3, ...\} \tag{2.64}$$

Both the methods have their advantages and their disadvantages. In general, the explicit methods are less stable and require a small time step compared to the implicit methods. The implicit methods on the other hand are computationally expensive as they require the solution of a matrix equation at each time step. Explicit methods are suitable when the flow is transient and turbulent because the time step required for resolution is small and they are less expensive and easy to program than their implicit counterparts. Implicit methods are suitable when the final flow is expected to be steady and a taking a larger time step allows for the solution to reach steady state faster even though the method is more expensive.

As the flow to be studied here is a turbulent, unsteady flow, we use explicit methods. The most well known explicit methods are the Runge Kutta family of methods.

2.4.2 Explicit Runge-Kutta methods

The general explicit Runge-Kutta method can be written as

$$U^{n+1} = U^n + \Delta t \sum_{i=0}^{s} b_i K_i \tag{2.65}$$

where the K_i's can be written as

$$\begin{aligned}
K_1 &= F(t_n, U^n) \\
K_2 &= F(t_n + c_2 \Delta t, U^n + \Delta t a_{2,1} K_1) \\
K_3 &= F(t_n + c_3 \Delta t, U^n + \Delta t a_{3,1} K_1 + \Delta t a_{3,2} K_2) \\
&\vdots \\
K_s &= F(t_n + c_s \Delta t, U^n + \Delta t a_{s,1} K_1 + \Delta t a_{s,2} K_2 + ... + \Delta t a_{s,s-1} K_{s-1})
\end{aligned} \tag{2.66}$$

where s is the number of stages the method uses. The constants c_i and $a_{i,j}$, $1 \leq i, j \leq s$ can be written in a tableau form called the Butcher Tableau as in Table 2.2.

Specifically the tableau for the Runge-Kutta 4th order method that has been used in this thesis is as in Table 2.3.

TABLE 2.2: Butcher Tableau

c_1				
c_2	$a_{2,1}$			
c_3	$a_{3,1}$	$a_{3,2}$		
$\vdots$	$\vdots$		$\ddots$	
c_s	$a_{s,1}$	$\dots$		$a_{s,s}$
	b_1	$\dots$		b_s

TABLE 2.3: Butcher Tableau - RK4

0				
$\frac{1}{2}$	$\frac{1}{2}$			
$\frac{1}{2}$	0	$\frac{1}{2}$		
1	0	0	1	
	$\frac{1}{6}$	$\frac{1}{3}$	$\frac{1}{3}$	$\frac{1}{6}$

For a detailed analysis of the stability analysis of the Runge-Kutta methods using Fourier analysis and stability plots that define the time step restrictions based on the CFL number, one can refer [44, 45].

2.5 Boundary conditions

For the solution of any differential equation, it is required to specify the boundary conditions and if the equation is time dependent, then it may also be necessary to specify a initial condition. In a numerical simulation due to restrictions on the memory and computation there is a truncation of the physical boundaries to create artificial boundaries which are not actually the boundary of the equation but a necessity for the simulation. Boundary conditions have been a corner stone of fluid mechanics and have been one of the most complicated aspects in the solution of the governing equations for a problem.

For direct numerical simulations which aim to simulate flows by resolving the small scales as well, accurate methods are essential. For these accurate methods, it is important that the boundary conditions be treated carefully. With the simulation of turbulent flows, it also becomes important to take care of waves and their reflections

at the boundaries. With unsteady flows, there is the added complexity that these waves cannot be dampened by the numerical dissipation and therefore other non-reflecting or absorbing boundary conditions have to used.

It has been explained by [46] and shown experimentally by many others [47, 48] that acoustic waves are important in turbulent flows and are coupled to many turbulent mechanisms. Therefore to capture these waves it is important to accurately control the behaviour at the boundaries.

As the well-posedness of the boundary conditions used are critical to the solution of any partial differential equation, this is quite important. This well-posedness has been shown for Euler equations by [49] and for some cases for the Navier–Stokes equation by [50].

Apart from the usual boundary conditions, for numerical implementations, numerical boundary conditions (compatibility relations) are sometimes required to solve for unknowns not specified at the boundaries.

Various types of boundary conditions have been developed by various authors:

1. Poinsot and Lele [46]: Developed general boundary conditions that give the number of boundary condtions that need to be implemented for well-posedness including the compatibility relations. Their methods used the characteristics of the equations and were called the Navier–Stokes characteristic boundary conditions (NSCBC) and were an extension of the methods by Thompson [51].

2. Bogey and Bailly [52]: Developed non-reflective boundary conditions to minimize acoustic reflections and also used a sponge layer to dampen the reflections.

3. Colonius et al [53]: Developed non-reflective boundary conditions for the non-linear NS equations and reducing the reflection at the outflow by using grid stretching and filtering.

4. Tam and Dong [54]: Developed radiation boundary conditions that allow for a smaller computational domain. These boundary conditions were also developed for acoustics therefore are meant to be non-reflective.

These are the variety of boundary conditions available but the ones that were used for the simulation will be elaborated on in section 3.4.

Chapter 3

Implementation and Tests

This chapter explains the implementation aspects and also shows some of the tests that demonstrate the ideas explained in Chapter 2. The objective of this chapter is to make the reader understand the implementation aspects, establish the proof of concept and validate the methods used in the simulation of the actual problem.

3.1 Implementation

The code was implemented in FORTRAN 77/90 and uses a combination of the features of both the standards. An Intel 2016 FORTRAN compiler was used.

3.1.1 Direct Numerical Simulation

Direct Numerical Simulation (DNS) involves the direct discretization of the governing equations without the use of any modeling. It differs from its counterparts LES, RANS and URANS in the aspect that all these methods use models to capture the effect of the smaller scales and transfer them to the larger scales (LES) or use an averaging procedure and a turbulence model to model the turbulent fluctuations (RANS).

From a physical perspective, DNS accurately captures the physics without modeling given enough computational power and time. For problems with very high Reynolds numbers the range of scales which need to be captured to obtain accurate flow characteristics also increases making DNS impractical due to the need for higher computational power. In these cases, LES and RANS methods are more suitable. This thesis

makes use of DNS to simulate the compressible turbulent jet. Though the DNS as a tool for industrial research is still not viable, it can be very valuable as a design tool for the models used for LES and RANS. It can also be used to test various discretization methods and compare them to experimental results for further use in other simulation paradigms.

3.1.2 Parallelization

Parallelization has been used in this thesis to speedup the computations. This parallelization has been done using the Message Passing Interface (MPI) libraries.

3.1.2.1 Message Passing Interface

MPI is a standard used for communication between different processes in a multi-process program and all the MPI libraries, OpenMPI, IntelMPI, MPICH etc., follow the standard. It outlines basic routines that allow for communication between the different processes working in parallel.

3.1.2.2 Implementation

The first aspect of parallelization is the decomposition of the domain and assignment of the different processes to the sub-divided domains. The code in this thesis uses the `2decomp` [1] pencil decomposition library to divide the domain as shown in Figure 3.1. As the problem in consideration is a 3D problem, there are 3 solves involved. In the x, y and z directions and are done sequentially. The x and the z solves are done with the domain in the left of the Figure 3.1. The data is then transposed such that there are no divisions perpendicular to the y domain as shown in the right side of the Figure 3.1.

3.1.2.3 Memory Requirements

Memory requirements can be divided into two parts: the memory required during the running of the code, which includes the memory of the various variables and fields

[1] :http://www.2decomp.org/index.html

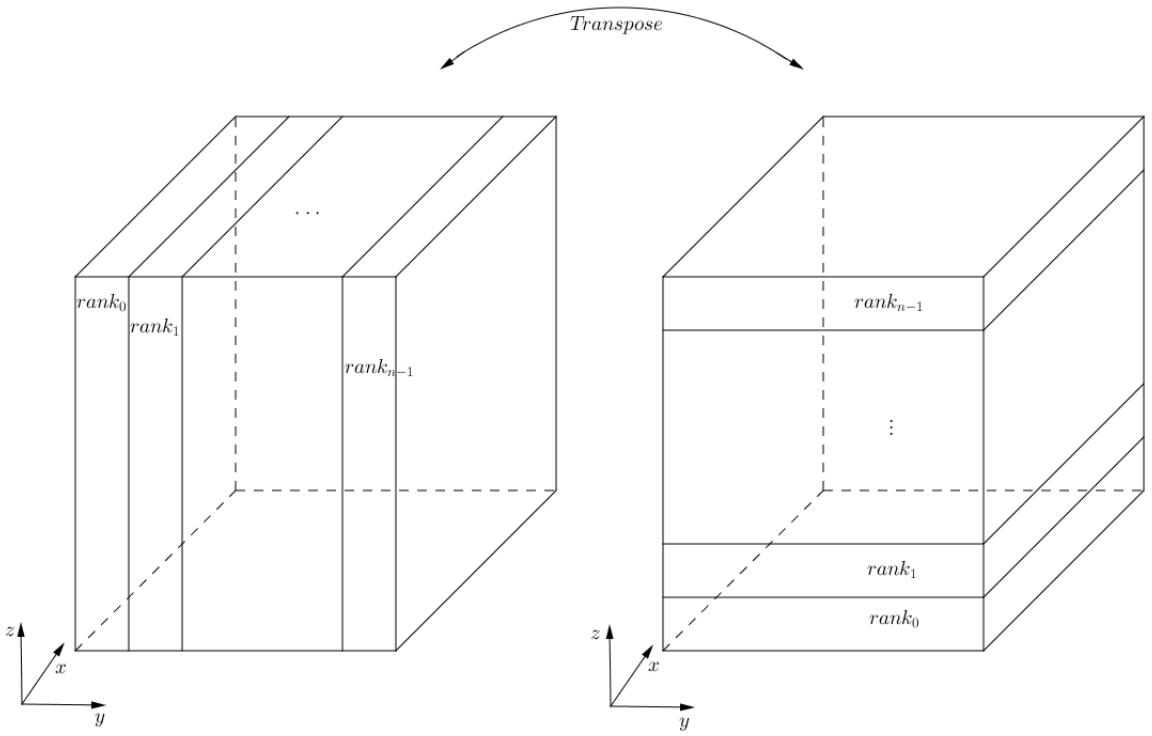

FIGURE 3.1: Domain Decomposition

which includes both the local and the global fields. The other one is the memory required to store the variables and fields required for post-processing.

Tests were performed on both using both single precision and double precision and single precision results were sufficiently close to the double precision results. Hence only single precision was used. This reduces the memory requirements and the computing time and hence is optimal.

If we consider the number of grid points as $n \times m \times l$, we see that we need to store the fields at each of these these grid points throughout the runtime of the program and output them for post-processing, if required.

The fields that need to be stored are: $u, v, w, p, T, e, Y_k, \rho$. Considering the overall number of grid points to be $N = n \times m \times l$. Each of the numbers being a single precision, `real`, requires 4 bytes of memory. Therefore the memory required for the global variables is $4 \times 8 \times N$ bytes. Adding the memory taken by the grid points values, and the fact that we are working on a staggered grid, the overall memory required scales as $\mathcal{O}(80N)$, where N is the number of grid points. This is the minimum memory that is required in the program. If all the temporary variables are considered, the memory required can increase upto $\mathcal{O}(120N)$, but these temporary variables and fields are

deallocated at the exit of a subroutine and therefore the memory is free again for the next subroutine.

3.1.2.4 Computing requirements and timings

As described earlier, for this thesis, a 12th order method is used for regular interpolation and calculating the derivatives. A fourth order method is used for the WENO interpolations. With great order of accuracy of methods comes great requirement for computing power. A strong scaling test shows the following timings.

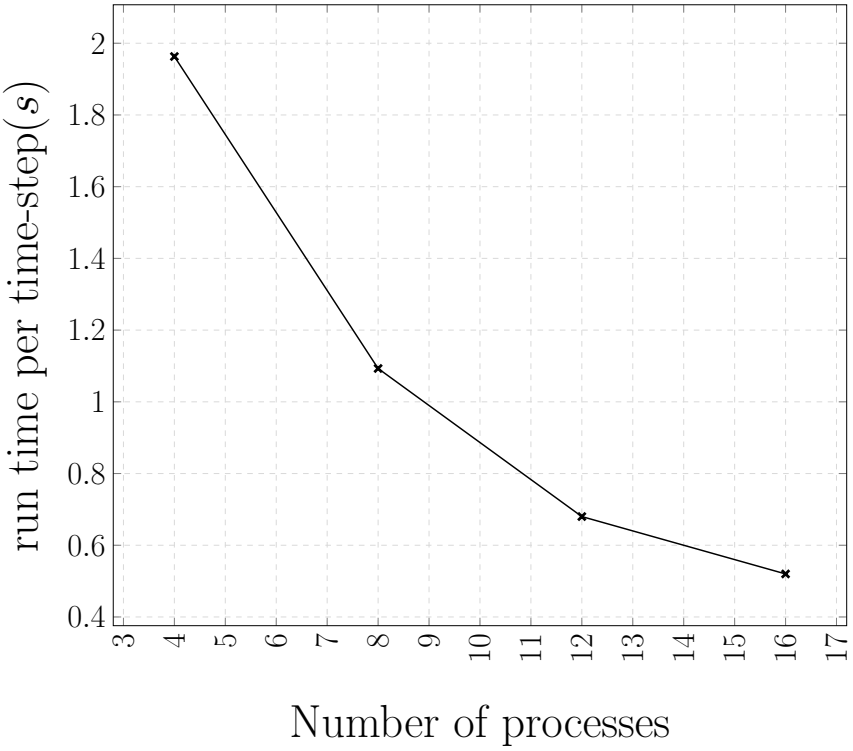

FIGURE 3.2: Strong scaling test, Problem size: $128 \times 64 \times 64$

We see that for a constant problem size, increasing the number of processes, reduces the run time per time step. The overall number of processes is bound by the computing limits and by the memory requirement of the entire program.

3.2 Discretization

This section elaborates on the implementation styles of the spatial and the temporal discretizations and the variations possible and their efficiencies with respect to computing time and memory.

3.2.1 Spatial discretization

This thesis uses the staggered schemes of Boersma [4] to differentiate each of the terms and to interpolate between the staggered and the co-located grids when needed. The scalars, ρ, e, T, Y_k are present on the cell centers whereas the vector fields, u, v, w are on the cell faces corresponding to the respective normal directions.

3.2.1.1 Conservation of mass

The mass conservation equation is given in Equation 2.3. This equation requires the spatial derivative of the mass fluxes, ρu_j with respect to the direction x_j. First the density is interpolated to the face in the direction of x_j, and multiplied with u_j to form the flux product. This is stored for further use. The term $\partial(\rho u_j)/\partial x_j$ is then calculated at the cell center. The equation is then stepped in time.

3.2.1.2 Conservation of momentum

The momentum equations are given in Equation 2.10. They are a set of three equations in the x, y, z directions. Two terms can be identified here: the convective terms, $\partial(\rho u_j u_i)/\partial x_j$ and the diffusive terms, $\partial(\tau_{ij})/\partial x_j$. For the convective term, $\partial(\rho u_j u_j)/\partial x_j$, the velocities, u_j's are interpolated to the cell centers and the derivative is computed at the cell faces. For the term $\partial(\rho u_j u_i)/\partial x_j$, the flux,$\rho u_j$ and velocity u_i are interpolated to the cell corner and the derivative is obtained at the cell face. The pressure gradient for the x momentum equation is calculated at the cell face directly as the values are already available at the cell centers. The diffusive terms are also calculated in a similar fashion where the role of the flux is taken by the first derivative. The terms are added and the equation is stepped in time to obtain the fluxes through which the velocities are then reconstructed.

3.2.1.3 Conservation of energy and scalars

Both the scalar conservation equations have two main terms, the convective terms and the diffusive terms. The convective terms, $\partial((E+p)u_j)/\partial x_j$ and $\partial(Y_k \rho u_j)/\partial x_j$ are calculated by interpolating the scalars, E, Y_k to the cell faces and multiplying with the velocities and calculating the derivative at the cell centers. The diffusive terms involve the calculation of a first derivative term of the scalar (T or Y_k), which is calculated at

cell face directly and multiplication of that with the diffusion coefficients, κ which is interpolated to the cell face and multiplied with the derivative previously calculated and the final derivative is calculated at the cell center. The last term for the energy equation includes a derivative term that models the energy diffusion by shear. The shear stress term, τ_{ij} is interpolated to the cell face and multiplied with the velocity, u_j and stored during the solution of the momentum equation. This term is then used here and the final derivative is calculated at the cell center.

For the scalar equation, the WENO method has been used to remove the oscillations that were occurring if solved without a non-oscillatory method. The WENO interpolation is required only for the convective terms in the scalar equation and before taking the derivative, the terms are interpolated through a WENO procedure. Therefore, for the convective terms of the form $\partial(Y_k \rho u_j)/\partial x_j$, the velocity, u_j is interpolated to the cell center and the product $Y_k \rho u_j$ is formed. This quantity is then interpolated using the WENO procedure as in Equation 2.56 to the cell faces and the derivative is calculated. As this is a convective term and the WENO interpolation involves stencils some of which are upwind(downwind) and that the convective velocity (ρu_j) can be positive or negative, we need to use a flux splitting method to use the appropriate stencils. This was done as shown in Equation 2.61 using the Lax-Friedrichs flux splitting. The convective velocity was the interpolated velocity (to the cell center) multiplied with the density. After the WENO interpolation the derivative of the term was taken using the compact finite difference method of Boersma.

The stencils for the WENO interpolations are centered about $x_{i+1/2}$. This means that at the left and right boundaries in all the three spatial directions, appropriate ghost values need to be calculated. This is done using a simple Lagrangian extrapolation procedure. This procedure is similar to the Lax-Wendroff procedure[55] which is a more generalized version of the Lagrangian extrapolation procedure. This Lagrangian extrapolation procedure has been explained in Appendix A.

3.2.2 Temporal discretization

The fourth order Runge Kutta method was used to advance the equations in time as given in Equation 2.65, specifically the RK4 method. For example, for the mass equation, all terms expect the one with the time derivative are first calculated and stepped through time with intermediate values as required.

The TVD-RK [56] was also experimented with for the scalar equation to improve stability, but no changes were observed in the results, hence all results shown are of the RK4 method.

For ease in programming, the time derivative in the Equation 2.16 was split so that instead of the concentration flux only the concentration could be calculated for. The time derivative of the density was used from the mass equation. The final equation is

$$\rho\frac{\partial Y_k}{\partial t} + Y_k\frac{\partial \rho}{\partial t} + \frac{\partial \rho u_j Y_k}{\partial x_j} = \frac{\partial}{\partial x_j}\left(\rho\kappa_{scal}\frac{\partial Y_k}{\partial x_j}\right) + \omega_k \tag{3.1}$$

from which the scalar concentration, Y_k was calculated for.

3.3 Grid

Two types of grids are possible: the non-uniform grid and the uniform grid. A non-uniform grid allows for stretching and a fine mesh in regions where a higher resolution is required and a coarse mesh where there is no interest, which allows for a higher efficiency.

A uniform grid on the other hand, can only have a single resolution capability and to capture a higher resolution, a finer mesh is required. For the compact finite difference method, it is necessary to have a mapping to a domain with a uniform grid as explained in Equation 2.23. This mapping unfortunately introduces transfer errors after the WENO interpolation has taken place and hence a non-uniform grid cannot be used when using a compact hybrid WENO interpolation yet. Hence, in this thesis a uniform grid has been used with a fixed step size which can vary with the direction, if required.

3.4 Boundary conditions

As we work in a cartesian grid, our domain is a box and hence we have six face boundaries. The left boundary along the x axis is the inflow boundary where the jet enters the domain through the nozzle. The domain starts at the exit of the nozzle and the nozzle is not a part of the domain. The right boundary along x is the outflow boundary. The four other faces form the walls and have normals that are perpendicular to the x direction.

This thesis makes use of the ambient boundary conditions in which the quantities at the boundaries are set to the far-field ambient values. This means that for the boundary condition to make sense and be physical, one has to either increase the domain size to allow for the physical region of influence of the jet to be far from the boundaries emulating the far-field region or one can use sponge layers and damping methods to reduce the abrupt change of the quantities when the boundaries are close to the physical region of influence of the jet.

In general the well known boundary conditions are as developed by Lele [46] and Thompson [51]. But these boundary conditions require a large domain when ambient conditions are used as they may produce reflections which can influence the solution. In this thesis, the basic idea of the boundary conditions being the same as Lele [46], additional damping layers were added to ensure that the solution was reflection free.

As given in [46], for a subsonic inlet, the boundary conditions are not well defined. Therefore, an artificial convection velocity is added to the axial velocity to make it locally supersonic. This is also done at the outflow where the flow is convected out of the domain axially with an additional axial velocity. This supersonic velocity at the inflow and the outflow means that the no other flow variables need to be specified at the outflow to obtain a well-defined problem. The artificial convection velocity is reduced to zero uniformly in the interior of the domain. The region where the artificial convection velocity is added is limited to a region very close to the inflow and the outflow of the domain so that the solution is not affected by it. At the boundaries whose normals are perpendicular to the axial direction, the flow variables are set to ambient conditions. Even though this is strictly not true, but due to computational and physical constraints to limit the domains, we impose this. As these boundaries are far away (effectively, due to the damping and sponge layers) from the region of influence of the jet, this condition still gives meaningful results. Additionally, damping layers are added to ensure that the reflection from the boundaries do not affect the solution.

The damping is done at the boundaries by adding

$$- A(x, y, z)(\mathfrak{Q} - \mathfrak{Q}_{tar}) \tag{3.2}$$

where A is a function that is small in the required damping layers and zero in the interior of the domain. $\mathfrak{Q}$ is the quantity to be damped for the equation being solved. For example for the conservation of mass, Equation 2.3, $\mathfrak{Q} = \rho$. The quantity $\mathfrak{Q}_{tar}$

is the time averaged quantity in the simulation. This time averaged quantity was calculated by averaging in both time and in the tangential space direction. If $\mathcal{A}_1$ consisted to time average of the previous n time steps, and $\mathcal{A}_2$ was the time average of the previous $n + n_0$ time steps, after n_0 steps, $\mathcal{A}_1$ was replaced by $\mathcal{A}_2$ and $\mathcal{A}_1$ was set to zero. This way an average of the quantities between n_0 and $2n_0$ was available.

3.4.1 Inflow boundary

At the left boundary, the jet enters the domain and hence an inflow profile for the jet is required. The inflow profiles used were based on [57] and were such that at the downstream of the flow (exit of the nozzle), the mean velocity profiles would match. The values for various quantities were defined as given in Equation 3.3

$$
\begin{aligned}
u &= \frac{Ma}{2}\left(1 - \tanh\left[B\left(\frac{r}{r_{jet}} - \frac{r_{jet}}{r}\right)\right]\right) \\
v &= 0.0 \\
w &= 0.0 \\
\rho &= 1 + \left(\frac{T_0}{T_{jet}}\right)\frac{u}{Ma} \\
E &= \frac{1}{\gamma(\gamma-1)} + \frac{1}{2}\rho u^2 \\
Y_k &= \begin{cases} 1.0 & , d \leq d_{jet} \\ 0.0 & , \text{else} \end{cases}
\end{aligned}
\tag{3.3}
$$

where d_{jet} is the jet diameter and d is twice the radial distance in the inflow plane from the center of the jet. B is a parameter that controls the shear layer thickness and is based on the momentum thickness. At a region very close to the inflow, small additional terms are added as well to force the jet to the inflow state. Though this is not physical, this region is restricted to a very small region near the inflow and hence the flow downstream remains physical as will be seen in the results.

Additionally at the inflow, perturbations are added to the flow to allow for the development of unstable modes. The method is similar to that described in [5]. These perturbations are directly added to the parameter B controlling the shear layer thickness and is as given in Equation 3.4

$$B = B(\theta, t) = B_0 + \sum_m \sum_n \mathfrak{B}_{nm} \cos(f_{nm}t + \phi_{nm}) cos(m\theta + \psi_{nm}) \tag{3.4}$$

where $\mathfrak{B}_{nm}, f_{nm}, \phi_{nm}, \psi_{nm}$ are the azimuthal modes that are randomly updated in time. B_0 is the jet shear layer thickness parameter that is based on the momentum thickness and is set to 8.0 for all simulations here.

3.4.2 Outflow boundary

Due to the supersonic inlet and the supersonic outlet boundary condition used, there is no need to specify additional flow variables at the outflow to obtain a well-defined problem. Additionally, the flow quantities are filtered to remove large fluctuations from affecting the solution quality. For a flow quantity F, the filtered quantity $\hat{F}$ is used obtain the new quantity as in Equation 3.5.

$$\begin{aligned} F^{new}(x,y,z) = F^{old}(x,y,z) + \\ 0.5(1 - \tanh[a_{fil}(x_{max} - x - x_{fil})])(\hat{F}^{old}(x,y,z) - F^{old}(x,y,z)) \end{aligned} \tag{3.5}$$

The values of a_{fil} and x_{fil} are set at 2.5 and 0.0 respectively for the simulations presented here. The filtered quantity, $\hat{F}$ was obtained by using a spatial filter which was a compact filter.

3.4.3 Lateral boundaries

For the lateral boundaries, the solution is specified at certain state. This may be the average state or the ambient state. To allow the solution to smoothly go to the specified state at the boundaries, damping or sponge layers are added as described earlier.

3.5 Numerical Tests

This section compares the different methods and shows the improvement possible due to the WENO methods. A simple test cases was considered, the advection equation.

3.5.1 The Advection equation

The advection equation as shown in Equation 3.6 is an important test case for all numerical methods as the exact solution is known and the behaviour is very well understood. Even though it is a simple linear equation, for some initial conditions, it can be quite difficult to accurately solve the equation.

$$\frac{\partial C_{test}}{\partial t} + u_{test}\frac{\partial C_{test}}{\partial x} = 0 \tag{3.6}$$

Two initial conditions were considered. One being a smooth initial condition, a sine wave and another being a square wave, with two sharp discontinuities. For both cases, the advection velocity, $u_{test} = 1.0$. The final time, $t_{end} = 10.0$. The number of grid points was equal to 100 for the square wave and 50 for the sine. The CFL number, CFL $= \frac{dt|u_{test}|}{dx}$ was set at 0.7. To emulate the effects of interpolation between the cell centers and cell faces in the problem, the values of C_{test} originally at the cell centers were interpolated to the cell faces. For just the compact finite differencing method, the derivative at the cell faces were taken to obtain the values of the derivatives at the cell centers. For the compact WENO methods, the cell face values were interpolated back to the cell centers and the final derivative was taken using the values from the cell centers and the cell faces as done by Liu et al. [21].

Figure 3.3 shows the comparison between the three schemes for the solution of the advection equation. The following observations can be made:

1. The compact finite difference scheme oscillates near the discontinuities which makes it unsuitable for problems with strong discontinuities, Figures 3.3(a),3.3(b). For a smooth initial condition, it behaves very well as can be seen from Figures 3.3(c),3.3(d).

2. The WENO 4^{th} order scheme does not oscillate either with the smooth initial condition or in the presence of strong discontinuities.

3. The WENO 6^{th} order scheme on the other hand can oscillate downstream of a discontinuity but behaves well upstream of a discontinuity. Though the order of the scheme is higher, these oscillations, even if very small make it unsuitable for the actual physical problem. These small oscillations were observed by Liu et al [21] as well.

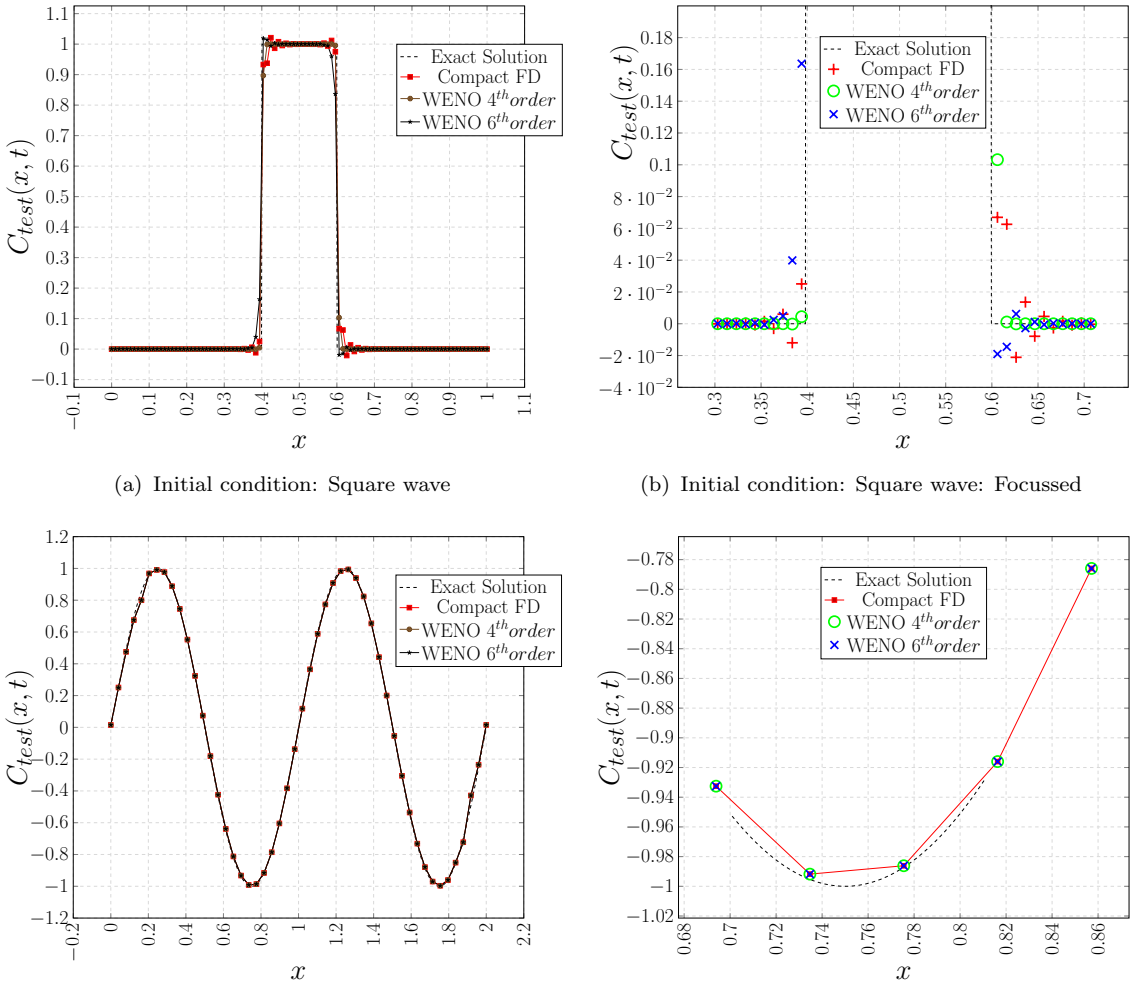

(a) Initial condition: Square wave

(b) Initial condition: Square wave: Focussed

(c) Initial condition: Sine wave

(d) Initial condition: Sine wave: Focussed

FIGURE 3.3: Numerical Tests: Comparison of WENO with central compact schemes

From the above test, we showed the need for the WENO methods and the situation in which WENO methods are required. As the computational effort required by the 4^{th} order interpolation is lesser than that of the 6^{th} order interpolation and that the 4^{th} order interpolation is stable and non-oscillatory, this thesis uses the 4^{th} order interpolation for all simulations.

Chapter 4

Scalar transport in turbulent jet

This chapter presents the simulation results and an analysis of the physics of the flow given specific flow conditions. First small cases are considered to show the effect of various numerical parameters and choose the optimal parameters. Finally, results are presented for the larger grid and some physical parameters are varied to obtain information about their effects on the flow and the results are compared with experiments and previous available simulations.

4.1 Need for a non-oscillatory method

Figure 4.1 compares the scalar fields just from compact finite difference to the ones with the compact WENO. From Figure 4.1 we can see that the compact FD method has a lot of oscillations around zero making the scalar concentration values near large gradients or discontinuities, unphysical. As a comparison, when a WENO interpolation is used, the oscillations vanish and we get a physical non-oscillatory solution. Therefore, at higher Reynolds numbers it is important to use a WENO method to remove the oscillations in the flow and accurately capture the discontinuities.

4.2 Numerical dependencies

This section tests the differences in the physical solution due to the numerical parameters. Three cases (4.2(a), 4.2(c),4.2(b)) are considered:

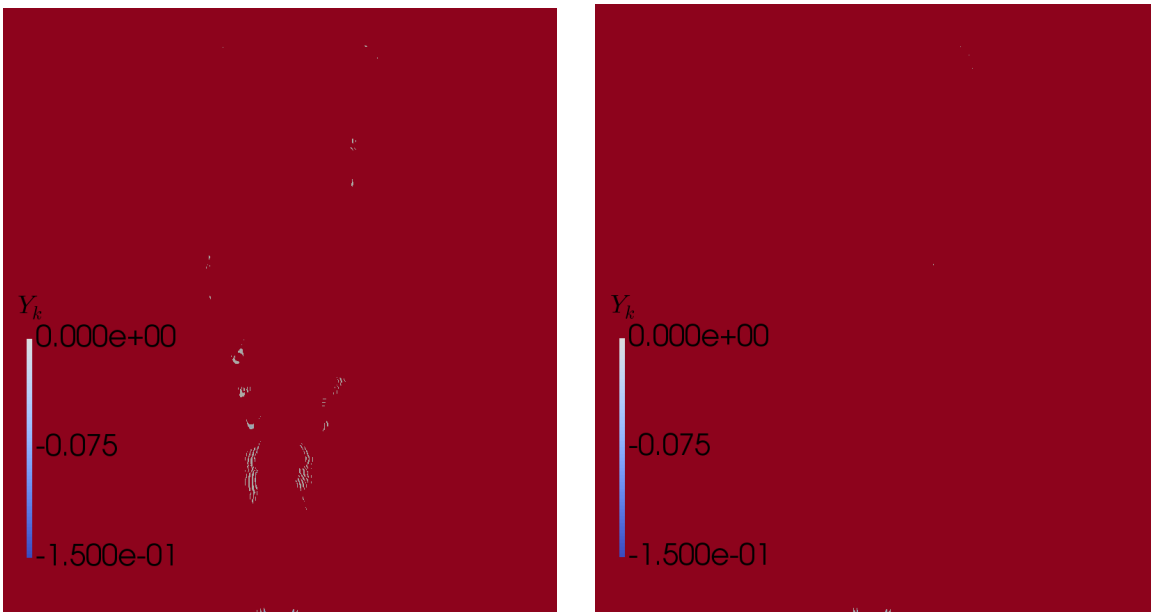

(a) Compact FD (b) Compact WENO

FIGURE 4.1: Oscillations in scalar concentration,Y_k fields, Re = 8500

1. Compact finite differencing: The scalar transport equation is solved using the compact finite difference method just as the rest of the equations.

2. WENO, low dissipation: The scalar equation is solved with an additional WENO interpolation but with low numerical dissipation. The numerical parameters were set as $\epsilon = 10^{-9}, C = 9.0, r_c = 0.1$. An explanation of the parameters has been given in section 2.3.

3. WENO, high dissipation: The scalar equation is solved with an additional WENO interpolation but with high numerical dissipation. The numerical parameters were set as $\epsilon = 10^{-6}, C = 5.0, r_c = 0.4$. An explanation of the parameters has been given in section 2.3.

4.2.1 Observations

The following observations were made from the numerical tests:

1. The Compact FD method, using effectively a central difference stencils had a lot of oscillations above the maximum possible concentration level and also negative concentrations which were unphysical.

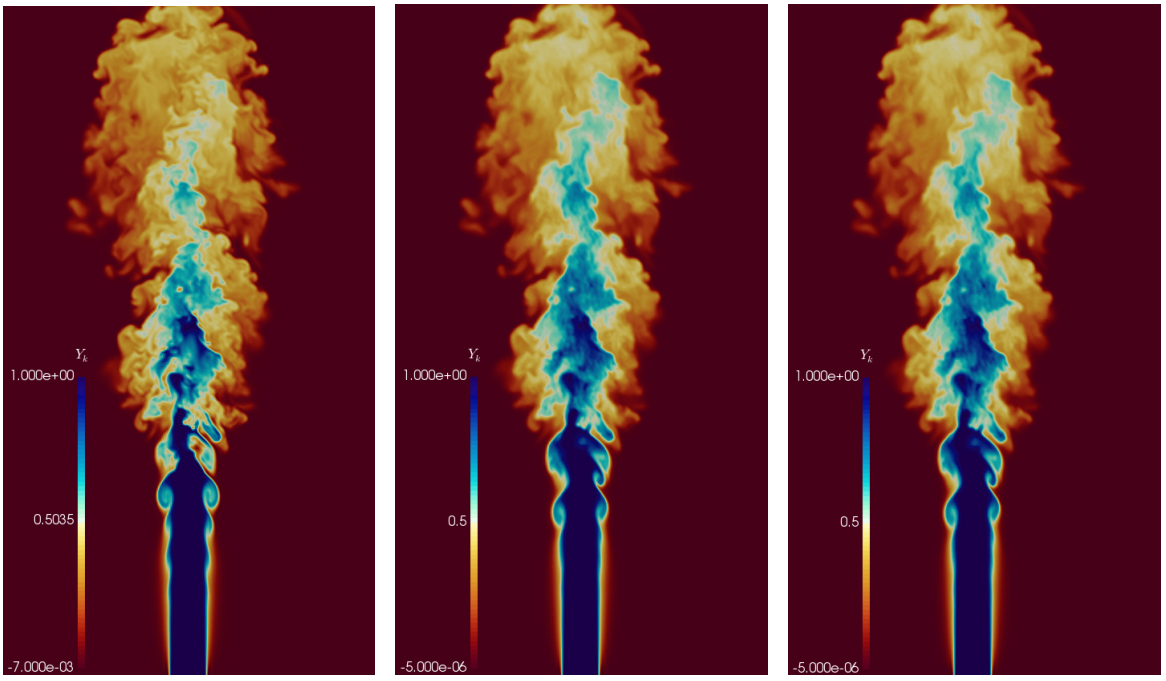

(a) Scalar concentration: Compact FD (b) Scalar concentration: WENO, low dissipation (c) Scalar concentration: WENO, high dissipation

FIGURE 4.2: Scalar concentration contours

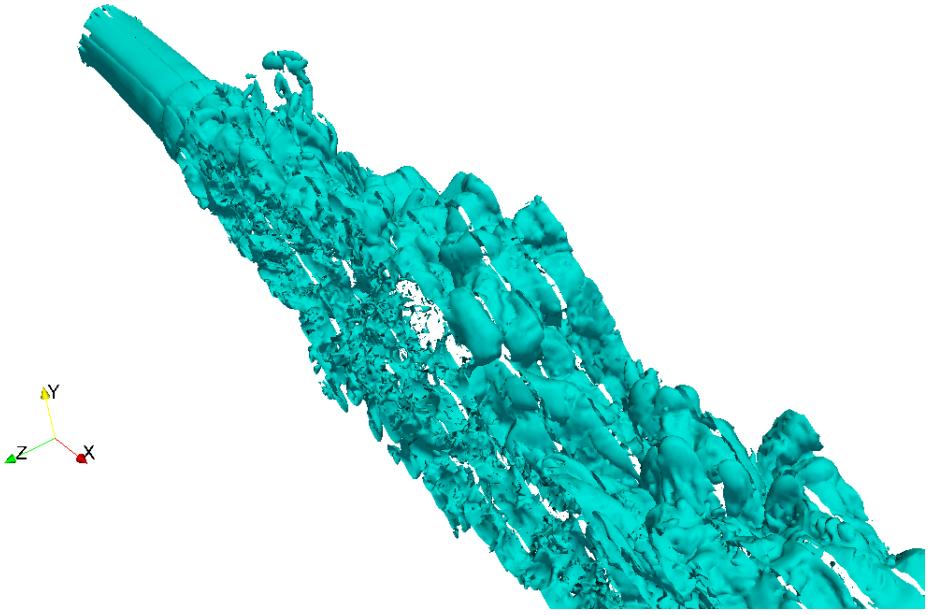

FIGURE 4.3: Iso-surfaces of vorticity

2. The concentration in the region close the jet axis falls sharply for the Compact FD method but not when WENO interpolation is used.

4.3 Validation

To ascertain the accuracy and validity of the results obtained, comparisons with existing literature was performed. The normalized averaged centerline velocity (NACV) of the current method with a resolution of $960 \times 480 \times 480$ with time step size $1/200$ and a CFL number of 0.5 was compared with experimental results given in [29] and [58]. The Reynolds number was set at 1×10^4 and the Mach number at 0.5, both of which were very close to the experimental conditions for the results in [29] and [58] .

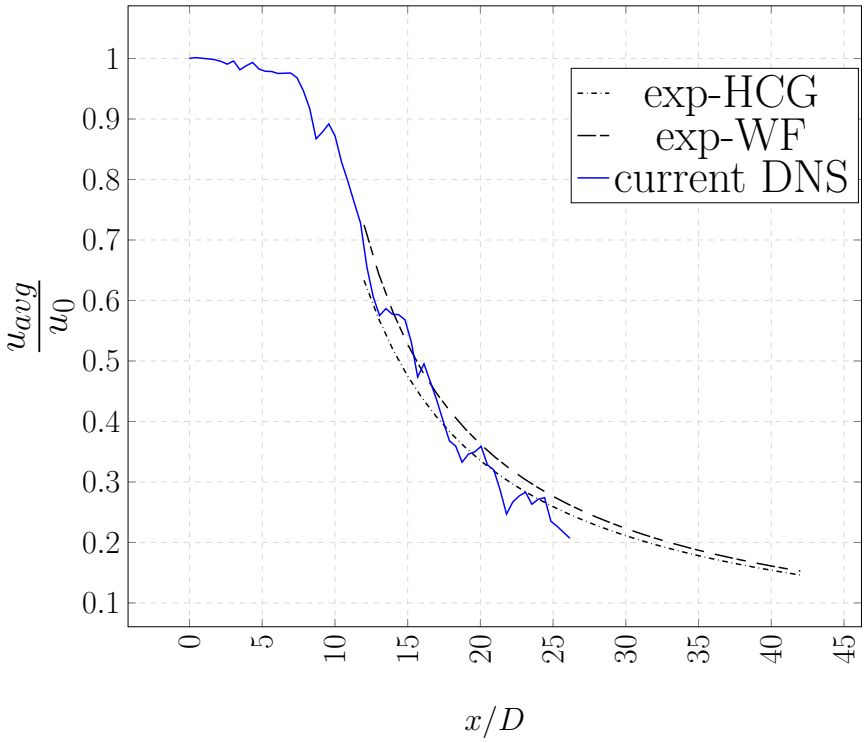

FIGURE 4.4: Comparison with experimental results at $\mathrm{Re} = 1 \times 10^4$, y normal

The Figure 4.4 shows that the centerline velocity matches pretty well with the experimental results. From this figure we can infer the following:

1. The potential core of the jet extends to about $x/D = 7$ for the current physical conditions.

2. The good agreeement with the experimental results shows that the spatial and temporal grid spacing are enough to capture the averaged statistical information

in the DNS study. Therefore, similar resolutions have been used in all simulations here on.

3. The trend in the NACV is $1/X$ which is as expected from the literature. A decay rate study has been performed next.

The trend in the NACV, $\frac{u_{avg}}{u_0}$ is $1/X$ where $X = x/D$. Then this implies that the inverse of the NACV, $\frac{u_0}{u_{avg}}$ will be a straight line in the field after the potential core. This allows us to estimate the slope of the curve hence a property of the flow to quantify its behaviour based on the physical parameters.

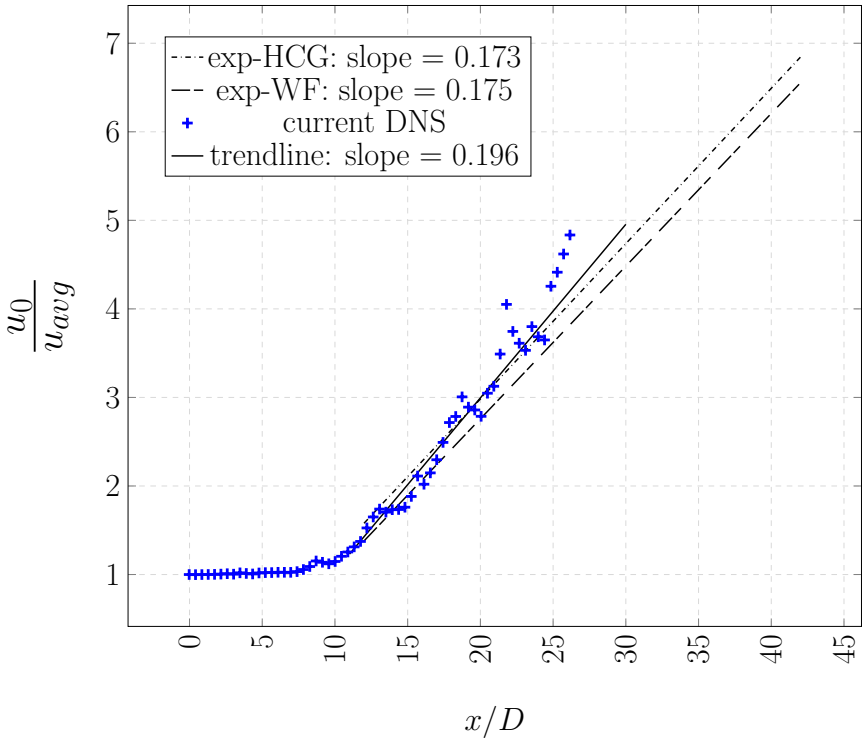

FIGURE 4.5: Comparison with experimental results at Re $= 1 \times 10^4$, decay rates, y normal

The decay rates calculate from Figure 4.5 are tabulated in Table 4.1

Method	***Decay rate (inverse of the slopes)***
Experimental, HCG [9]	5.78
Experimental, WF [9]	5.71
Current DNS	5.11

TABLE 4.1: Decay rates of NACV at Re $= 1 \times 10^4$

We see that the expected decay rates are between 5.0 and 5.9 as given in [59]. The decay rates observed here as well in other numerical simulations are lower than those of their experimental counterparts.

4.4 Final observations and results

This section compares the compressible turbulent jet at a moderately high Reynolds number of 8500, high Mach number of 0.9 and Schmidt numbers of 0.5 and 1.0. Some observations are noted and based on the observations some final conclusions are drawn.

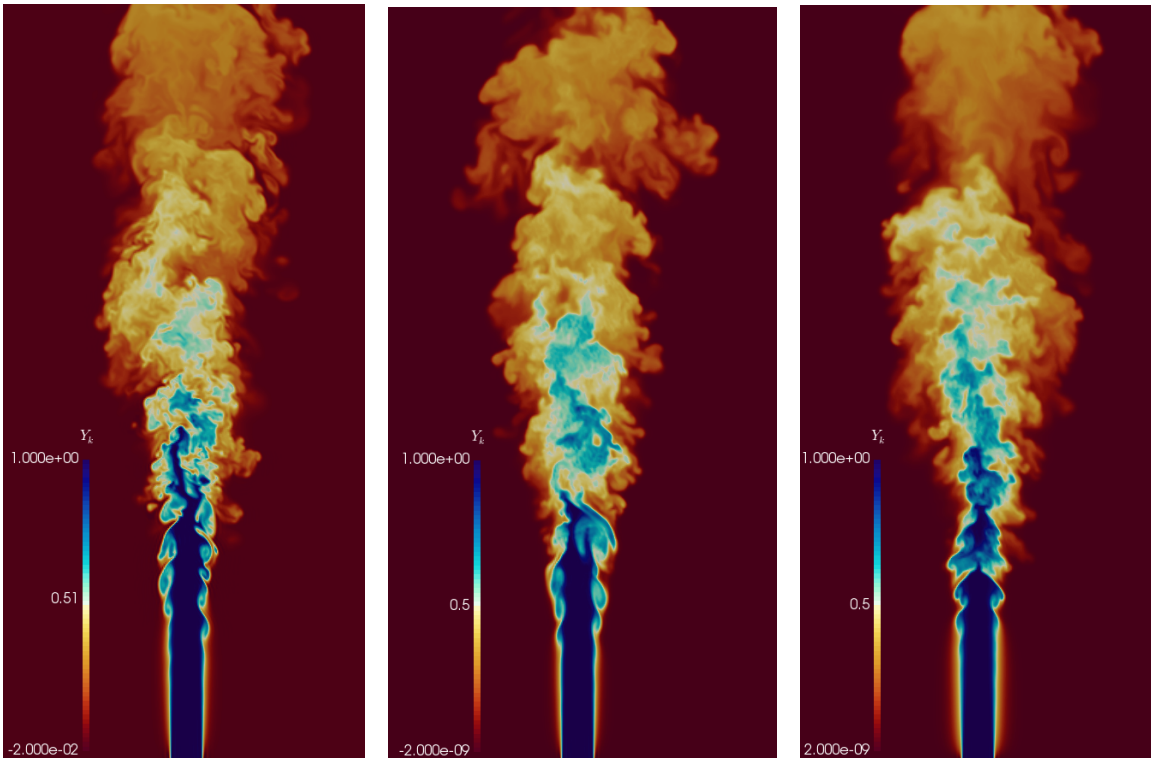

(a) Compact FD, Sc = 1.0 (b) Compact WENO, Sc = 1.0 (c) Compact WENO, Sc = 0.5

FIGURE 4.6: Scalar concentration,Y_k fields, Re = 8500

4.4.1 Observations

The Figure 4.6 shows the scalar concentration fields for three different simulations. Two are for the same physical conditions and the methods of simulation are different, being the compact finite difference method and the WENO method and the last one

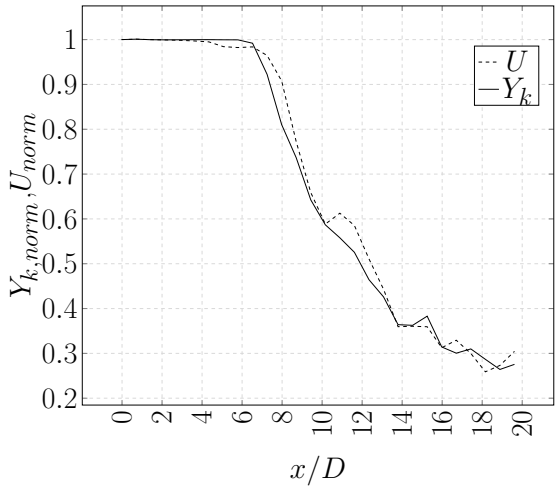

(a) Compact FD, Sc = 1.0

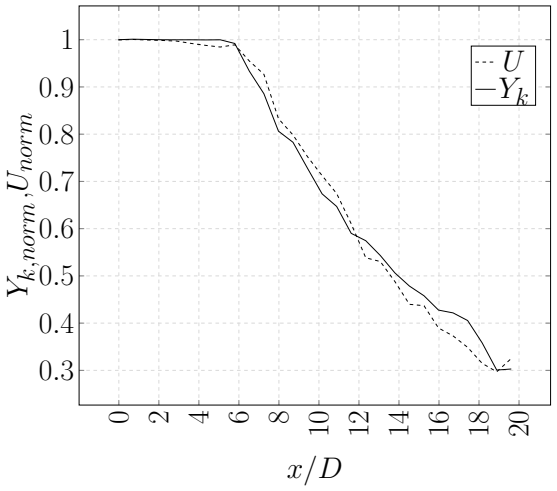

(b) WENO, Sc = 1.0

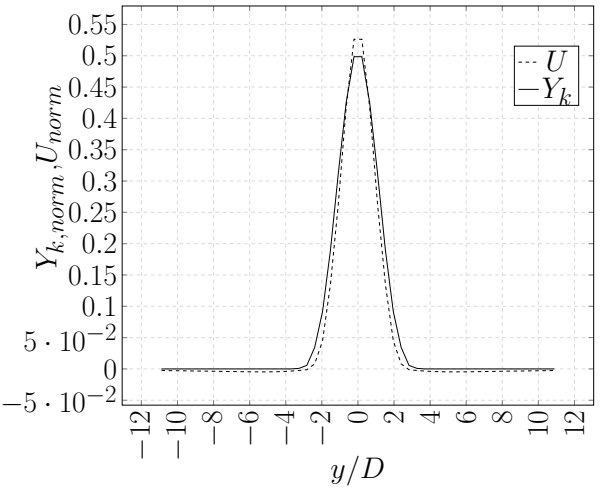

(c) Compact FD, Sc = 1.0, at $x/D = 12$

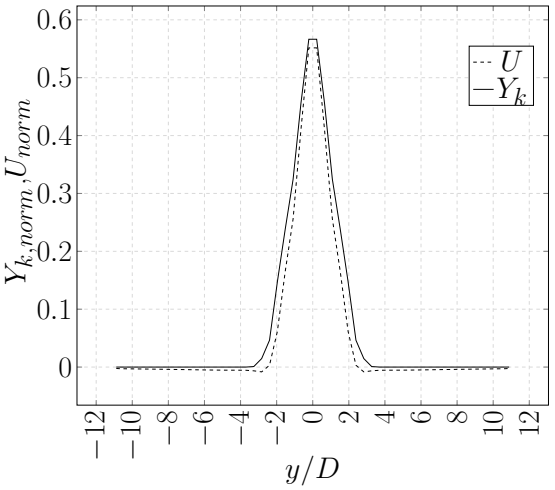

(d) WENO, Sc = 1.0, at $x/D = 12$

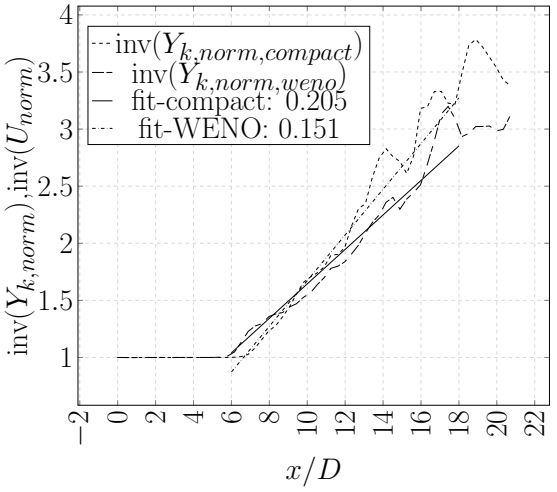

(e) Decay rate comparsion

FIGURE 4.7: Comparison of Compact FD with WENO at Re = 8500 and Sc = 1.0

for a smaller Schmidt number to see the effect of Schmidt number on the concentration field. In Figure 4.7, $Y_{k,norm} = Y_{k,avg}/Y_{k,0}$, $U_{norm} = u_{avg}/u_0$, where u_{avg} was the averaged centerline velocity and $Y_{k,avg}$ was the averaged centerline concentration. The following observations were made:

1. We can observe that the instability modes that dominate the initial evolution of the jet is the helical mode for both the compact FD and the compact WENO method as expected for a higher Schmidt number.

2. It can also be observed that the compact FD has sharp transitions whereas the compact WENO has smoother transitions.

3. The behaviour of the Normalized Averaged Centerline Concentration (NACC) was found to be very similar to that of the NACV as expected and a $1/X$ behaviour was observed which closely followed the NACV curves.

4. For the same Schmidt numbers, the compact FD method had a lower decay rate than its compact WENO counterpart as seen from Table 4.2. This higher decay rate in WENO is as expected for a normalized averaged scalar concentration as observed in [9].

5. The distance from the inflow at which the NACV and the NACC reduced to 30% of initial value was about $x = 16D$ for the compact FD method and $x = 18D$ for the compact WENO method.

6. A Gaussian type profile was observed for a concentration profile taken perpendicular to the axis at a certain x/D. It was also observed that the compact WENO followed the velocity profile more closely than the compact FD method.

7. The potential core region, the region close to the inflow and the centerline axis which has both the NACC and NACV close to 1.0 extends to about $x/D = 6$ in both the compact FD and the compact WENO cases.

Method	***Decay rate***
Compact FD	4.89
Compact WENO	6.62

TABLE 4.2: Decay rates of NACC at Re $= 8.5 \times 10^3$, Sc $= 1.0$

In Figure 4.8, a comparison for two Schmidt numbers, $Sc = 1.0$ and $Sc = 0.5$ has been done. Figures 4.6(b) and 4.6(c) show the scalar concentration fields. The following observations can be made:

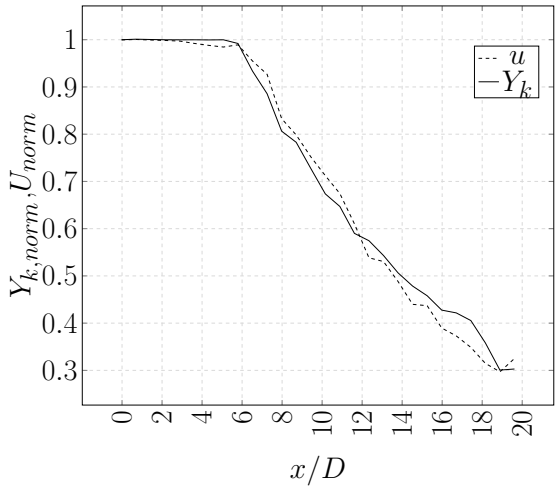

(a) WENO, Sc = 1.0

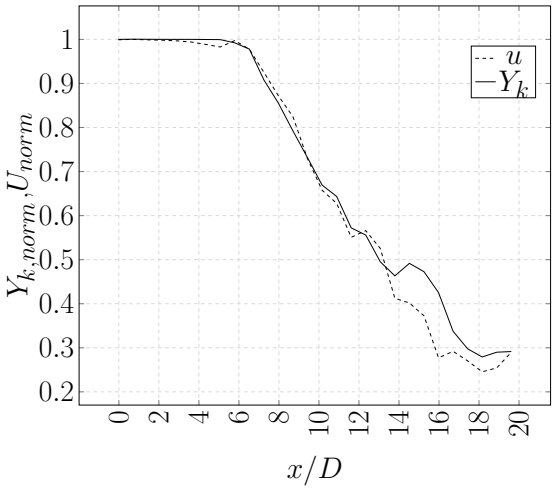

(b) WENO, Sc = 0.5

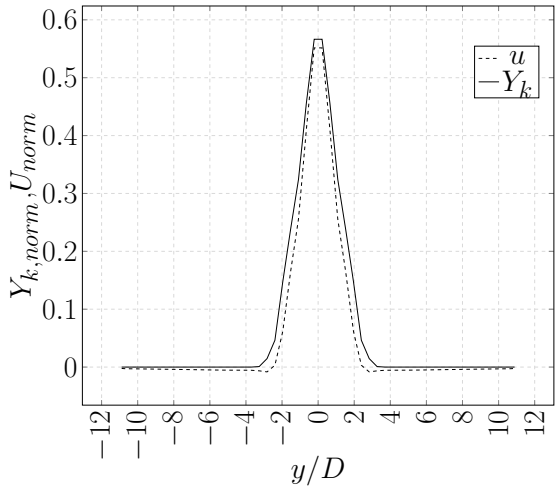

(c) WENO, Sc = 1.0, at $x/D = 12$

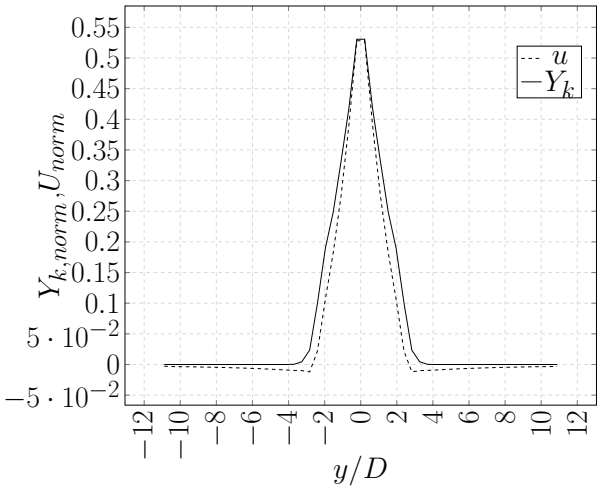

(d) WENO, Sc = 0.5, at $x/D = 12$

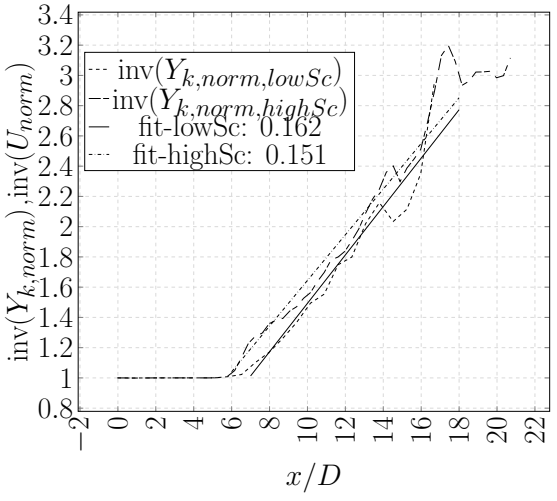

(e) Decay rate comparsion

FIGURE 4.8: Comparison of WENO at Sc = 0.5 and Sc = 1.0 at Re = 8500

1. We can see that the scalar fields in Figures 4.6(b) and 4.6(c) have different behaviour even though their averaged statistical behaviour is similar. For a higher Schmidt number, the dominating instability modes are helical whereas for a lower Schmidt number, the instability modes are varicose close to the potential core. Eventually, the high order helical modes break up the shear layer of the jet into coherent structures which merge and interact in a non-linear way downstream. These instability modes are linear and as described in [60] and in [61] and only either the varicose mode or the helical mode can dominate the initial evolution of the jet.

2. For the lower Schmidt number case, the decay rate is lower than that of the higher Schmidt number case as shown in Table 4.3 and in Figure 4.8(e).

3. The Gaussian like profile observed has a wider base for the higher Schmidt number case than for the lower Schmidt number case.

Method	***Decay rate***
Compact WENO, Sc = 1.0	6.62
Compact WENO, Sc = 0.5	6.17

TABLE 4.3: Decay rates of NACC at Re $= 8.5 \times 10^3$

4.4.2 Inferences and explanations

The above observations can be explained by:

1. The potential core of the jet, the region close to the inflow and the jet axis is the region in which no mixing occurs for the case of when more than one species exist. The flow is more or less directly advected downstream in the potential core. Downstream of the flow, the potential core breaks down, going from a laminar flow to a fully turbulent flow as evident from the increase in magnitudes of the cross-axis velocity (v, w) gradients.

2. The two main class of modes of instabilities are the symmetrical mode ($m = 0$) and the the asymmetrical modes ($m = \pm 1, \pm 2...$) which are higher order instabilities. The important modes of instabilities in the flow are generally the varicose mode ($m = 0$) and the helical mode ($m = \pm 1$) [61]. In this thesis, instabilities were added to flow according to Equation 3.4 with components which were randomly updated in time. The instability modes are dependent on the

inflow profile and the shear layer thickness. As the axial velocity reduces in the flow in the downstream at the near end of the potential core region, the shear roll-up occurs and we see a Kelvin-Helmholtz type instability. Depending on the physical conditions and the parameters, either the symmetrical instability mode or the asymmetrical mode dominate in the potential core end region breaking the shear layer into coherent structures and defining the evolution of the jet downstream.

3. The sharp transitions observed in the compact method are due to the oscillations produced by the method near large gradients. These oscillations produce unphysical values of the concentration and are hence undesirable. These sharp transitions are removed in the compact WENO methods.

4. The length of the potential core region depends on the type of instability breaking the shear layer and is hence dependent on the Reynolds number and the Mach number. Hence, this length is same in both the compact FD and the compact WENO methods.

5. A linear spreading rate implies a $1/X$ profile for both the concentration and the axial velocity. As the jet spreads the axial velocity decreases as one moves away from the jet centerline. This gives a Gaussian type profile as observed above.

6. The centerline, i.e $y/D = 0$ has the maximum axial velocity and therefore the maximum concentration value due to the linear spreading. As we move downstream, the magnitude of the axial velocity decreases as a result of the increase in the jet half-radius and the Gaussian profile dampens to zero in the far-field of the jet inflow as expected for a free turbulent flow.

7. The Schmidt number is the ratio of momentum diffusivity to the mass diffusivity. A Schmidt number equal to 1 tells us that the mass diffusivity is equal to the momentum diffusivity which is governed by the viscosity. A Schmidt number less than 1 means that the mass diffusivity of the species being transported is higher than the momentum diffusivity governed by the fluid viscosity. This means that the diffusion due to the viscosity is lesser than that of the species diffusivity making the flow in a manner less viscous for the species. Therefore, the decay rate in the scalar field is lesser even though the axial velocity velocity is higher.

8. This lower spreading rate in the lower Schmidt number case also means a narrow Gaussian profile for the scalar concentration field at a certain y/D value compared to the higher Schmidt number case.

Chapter 5

Conclusions and Future work

This chapter provides a conclusion to the work and summarizes the results and observations of the thesis. It also presents the reader with ideas for future work possible to develop on the results and ideas presented in the thesis.

5.1 Conclusions and recommendations

From the results and inferences above, the following conclusions can be drawn.

1. Scalar transport in a compressible turbulent jet at moderately high Reynolds numbers cannot be accurately modeled by a central compact method as it produces oscillations which are unphysical.

2. A non-oscillatory method is needed to remove the unphysical oscillations that are characteristic in the compact method near large gradients.

3. To reduce the numerical dissipation and increase the order of accuracy, a Weighted Essentially Non-Oscillatory (WENO) method should be used in place of the Essentially Non-Oscillatory (ENO) methods.

4. To further reduce the numerical dissipation, a hybridization of the central compact finite difference method and the WENO stencils should be used. This allows for accurate capture of discontinuities near large gradients while preserving order of accuracy and reducing the dissipation near smooth regions which is important in DNS to capture the behaviour and effects of small scales.

5. Though a high dissipation allows for no oscillations, it also adds a numerical viscosity to the solution. Therefore, if possible, to reduce the numerical viscosity, dissipation can be reduced by setting the parameters appropriately and increasing the domain size to reduce the oscillations. If one can only use a small domain and grid, then high dissipation parameters can be set to reduce the unphysical oscillations.

6. The potential core of the jet is the region where no mixing occurs for a multi-species flow and the length of the potential core depends on the physical non-dimensional parameters.

7. The normalized centerline averaged velocity of a compressible free turbulent jet decays along the jet centerline and its inverse shows a linear behaviour with a fixed slope that is dependent on the physical parameters.

8. The normalized averaged concentration also follows a similar axial decay as the axial averaged velocity that is governed by the physical parameters and on the evolution of the velocity field. The WENO method also accurately captures this behaviour.

9. The instability modes that dominate the evolution of the jet either for the velocity field or the concentration field are dependent on the inflow velocity profile and on the shear layer thickness parameter and on the physical non-dimensional numbers. Even though there are symmetrical and asymmetrical modes of instability only one type of mode dominates the evolution of the jet.

5.2 Future work

This current thesis may be improved upon with the following ideas and implementations:

1. A non-uniform mesh equivalent implementation for the WENO method would allow for the WENO method to work more efficiently.

2. An adaptive mesh refinement may be useful to increase the resolution and capturing the small scales that become important at the higher Reynolds numbers. An adaptive mesh would also be useful in reducing the numerical dissipation in the flow by restricting the upwind stencil usage in regions only containing the large gradients. It would also increase the efficiency of the code.

3. A grid independence study could provide insight into the dependence of the solution on the resolution required to accurately capture the smallest scales and the accuracy of the solution that does not capture these smaller scales.

4. A adjoint based sensitivity analysis could provide an insight into the effects of the non-dimensional parameters on the jet.

5. The code and method used in this thesis can be extended easily to solve for multiple species and for flows involving reactive species.

Appendix A

Lagrangian Extrapolation

At the left and right boundaries for each direction, WENO interpolation stencils require information which is actually physically non-existent. Therefore, a Lagrangian extrapolation procedure is used to calculate the values in these ghost cells.

The idea of Lagrangian interpolation/extrapolation is to calculate the values at the required known points given the known function values at certain points. Therefore, if we have y_k points which are the values of some function f at the given points x_k, our aim is to estimate the value at the required point x. If we denote the value to be interpolated or extrapolated as y, we can use a Chebyshev system of order n, $\{\phi_0, \phi_1, ..., \phi_n\}$, a orthogonal basis to obtain a unique function for the interpolant which can be written as

$$F_n = \sum_{k=0}^{n} y_k l_{k,n}(x) \tag{A.1}$$

We know that the Lagrangian interpolation should give us the function values at the given points. Therefore,

$$l_{k,n}(x_j) = \delta_{jk} \qquad\qquad j = 0, ..., n \tag{A.2}$$

Using the Chebyshev system to construct the function $l_{k,n}(x)$ we first define the determinant

$$D(x_0, ..., x_n) = \begin{vmatrix} \phi_0(x_0) & \cdots & \phi_n(x_0) \\ \vdots & & \vdots \\ \phi_0(x_n) & \cdots & \phi_n(x_n) \end{vmatrix}$$

And we define

$$l_{k,n}(x) = \frac{D(x_0, ..., x_{k-1}, x, x_{k+1}, ..., x_n)}{D(x_0, ..., x_{k-1}, x_k, x_{k+1}, ..., x_n)} \tag{A.3}$$

Taking the set of the Chebyshev polynolmials to be the set of monomials, $\{1, x, ..., x^n\}$, we can write the Lagrange interpolation polynomial as

$$l_{k,n}(x) = \frac{(x - x_0) \cdots (x - x_{k-1})(x - x_{k+1}) \cdots (x - x_n)}{(x_k - x_0) \cdots (x_k - x_{k-1})(x_k - x_{k+1}) \cdots (x_k - x_n)} \tag{A.4}$$

Therefore at a required x, the value of the interpolant/extrapolant, y is obtained as

$$y = L_n(x) = \sum_{k=0}^{n} y_k l_{k,n}(x) \tag{A.5}$$

Appendix B

Compact Finite Difference coefficients

The formula used to calculate the derivatives is as given in Equation 2.21

$$\begin{aligned}\alpha(f'_{i-1} + f'_{i+1}) + f'_i = d\frac{f_{i+7/2} - f_{i-7/2}}{h} + c\frac{f_{i+5/2} - f_{i-5/2}}{h} \\ +b\frac{f_{i+3/2} - f_{i-3/2}}{h} + a\frac{f_{i+1/2} - f_{i-1/2}}{h}\end{aligned} \tag{B.1}$$

The values of the coefficients can be obtained by matching the Taylor series expansions around grid point i and the uniform grid step size is given by ΔX. The coefficients are the same as in [4] and for the 10th order method are given by

$$\alpha = \frac{49}{140}, a = \frac{12985}{14592}, b = \frac{78841}{364800}, c = \frac{-343}{72960}, d = \frac{129}{851200} \quad \mathcal{O}(\Delta X^{10}) \tag{B.2}$$

Closer to the boundary the stencils are made smaller and successively lower order methods are used. Setting $d = 0$, we get and 8th order method,

$$\alpha = \frac{25}{118}, a = \frac{2675}{2832}, b = \frac{925}{5664}, c = \frac{-16}{28320}, d = 0 \quad \mathcal{O}(\Delta X^{8}) \tag{B.3}$$

Closer to the boundary, 6th and 4th order methods are used respectively,

$$\alpha = \frac{9}{62}, a = \frac{63}{62}, b = \frac{17}{186}, c = 0, d = 0 \quad \mathcal{O}(\Delta X^{6}) \tag{B.4}$$

$$\alpha = \frac{1}{22}, a = \frac{12}{11}, b = 0, c = 0, d = 0 \quad \mathcal{O}(\Delta X^4) \tag{B.5}$$

And finally at the boundary a one sided third order formulation is used to give

$$23f'_{i+1} + f'_i = \frac{1}{\Delta X}\left(-25f_{i+1/2} + 26f_{i+3/2} - f_{i+5/2} \right) \tag{B.6}$$

We also require an interpolation formula to appropriately interpolate the required data from the staggered grid to the co-located and vice versa. As this is also achieved using a compact interpolation formula, the coefficients and the formula are as follows.

$$\begin{aligned} \alpha(f_{i-1} + f_{i+1}) + f_i = a(f_{i+1/2} + f_{i-1/2}) + b(f_{i+3/2} + f_{i-3/2}) \\ +c(f_{i+5/2} + f_{i-5/2}) + d(f_{i+7/2} + f_{i-7/2}) \end{aligned} \tag{B.7}$$

$$\alpha = \frac{7}{18}, a = \frac{1225}{1536}, b = \frac{49}{512}, c = \frac{-7}{1536}, d = \frac{1}{4608} \quad \mathcal{O}(\Delta X^{10}) \tag{B.8}$$

Closer to the boundary the stencils are made smaller and successively lower order methods are used. Setting $d = 0$, we get an 8th order method,

$$\alpha = \frac{5}{14}, a = \frac{25}{32}, b = \frac{5}{64}, c = \frac{-6}{448}, d = 0 \quad \mathcal{O}(\Delta X^8) \tag{B.9}$$

Closer to the boundary, 6th and 4th order methods are used respectively,

$$\alpha = \frac{3}{10}, a = \frac{3}{4}, b = \frac{1}{20}, c = 0, d = 0 \quad \mathcal{O}(\Delta X^6) \tag{B.10}$$

$$\alpha = \frac{1}{6}, a = \frac{2}{3}, b = 0, c = 0, d = 0 \quad \mathcal{O}(\Delta X^4) \tag{B.11}$$

And finally at the boundary a one sided third order formulation is used to give

$$f_i = \frac{15}{8}f_{i+1/2} - \frac{5}{4}f_{i+3/2} + \frac{3}{8}f_{i+5/2} \tag{B.12}$$

Appendix C

A fun test case

All of us have been in a situation where we have had the misfortune of being downstream of someone who has broken wind. This fun exercise uses the statistical characteristics observed in this thesis to calculate the distance you must be from the person to not let your olfactory system identify the originator's food preferences.

The following assumptions were made to simplify the calculations:

1. The orifice is circular for simplicity.
2. No cross, tail or head winds that affect the flow.
3. The gas is mostly air with a initial small concentration of odorous gas with less than 10 % of the overall concentration by mass.
4. Based on a brief Internet search, the average concentration required for the olfactory system to sense the gas was assumed to be around 1 $\mu g/m^3$.
5. Again, based on some Internet sources, the velocity of the gas exiting the orifice was assumed to be around 15 m/s but the calculations can be performed with velocity as a parameter.
6. Based on Internet sources, the diameter of the orifice was assumed to be around 1 cm.
7. We have seen that the decay rate of a jet for concentration is higher than that of the velocity and is assumed to be about 6.6 here.

As the idea is to make sure that we do not smell the gas, we must keep ourselves at a distance far enough such that the concentration of the gas is low enough that it remains below the level that can be sensed by a human nose.

We know from the simulations that the simplified version for the centerline scalar concentration can be written as

$$C(x) = \frac{6.6}{x} \tag{C.1}$$

Using, this equation, we see that the concentration levels are below 1% of the original concentration level at a distance of $660D$, where D is the diameter of the orifice.

As the flow is a free turbulent jet the maximum concentration is at the centerline and at any radius perpendicular to the centerline a Gaussian type profile dictates the concentration levels. The $1/X$ behaviour is only observed after the potential core region which is approximately $6D$. Therefore, for the smell to remain undetected and below 1% of the original concentration, the victim has to be at least 666D away from the point of origin.

Of course all the above calculations are very simplified and the flow is much more complex but one can be almost sure that if one maintains a personal space of 660D around oneself, one can stay safe, unless with some misfortune, there is a headwind at the point of origin at which the only solution is to run like the wind.

Bibliography

[1] C Fukushima, L Aanen, and J Westerweel. Investigation of the Mixing Process in an Axisymmetric Turbulent Jet Using PIV and LIF. *Laser techniques for fluid mechanics*, pages 1–11, 2002. doi: 10.1007/978-3-662-08263-8.

[2] F T M Nieuwstadt, B J Boersma, and J Westerweel. *Turbulence: Introduction to theory and application of turbulent flows*. Springer-Verlag, 1st edition, 2015. ISBN 9783319315973.

[3] A Agrawal, B. J. Boersma, and A K. Prasad. Direct numerical simulation of a turbulent axisymmetric jet with buoyancy induced acceleration. *Flow, Turbulence and Combustion*, 73(3-4):277–305, 2005. ISSN 13866184. doi: 10.1007/s10494-005-8051-1.

[4] B J Boersma. A staggered compact finite difference formulation for the compressible Navier-Stokes equations. *Journal of Computational Physics*, 208(2):675–690, 2005. ISSN 00219991. doi: 10.1016/j.jcp.2005.03.004.

[5] J B. Freund. Noise sources in a low-Reynolds-number turbulent jet at Mach 0.9. *Journal of Fluid Mechanics*, 438:277–305, 2001. ISSN 0022-1120. doi: 10.1017/S0022112001004414.

[6] B J Boersma. Numerical simulation of the noise generated by a low Mach number, low Reynolds number jet. *Fluid Dynamics Research*, 35(6):425–447, 2004. ISSN 01695983. doi: 10.1016/j.fluiddyn.2004.10.003.

[7] P Moore, H Slot, and B J Boersma. Simulation and measurement of flow generated noise. *Journal of Computational Physics*, 224(1):449–463, 2007. ISSN 00219991. doi: 10.1016/j.jcp.2007.04.006.

[8] J B. Freund, S. K. Lele, and P Moin. Numerical simulation of a Mach 1.92 turbulent jet and its sound field. *AIAA Journal*, 38(11):2023–2031, 2000. ISSN 0001-1452. doi: 10.2514/3.14646.

[9] C. L. Lubbers, G. Brethouwer, and B. J. Boersma. Simulation of the mixing of a passive scalar in a round turbulent jet. *Fluid Dynamics Research*, 28(3):189–208, 2001. ISSN 01695983. doi: 10.1016/S0169-5983(00)00026-5.

[10] A Harten, B Engquist, S Osher, and S R. Chakravarthy. Uniformly high order accurate essentially non-oscillatory schemes, III. *Journal of Computational Physics*, 71(2):231–303, 1987. ISSN 10902716. doi: 10.1016/0021-9991(87)90031-3.

[11] C W Shu. Efficient Implementation of Essentially Non-oscillatory Schemes , II. *Journal of Computational Physics*, 78:32–78, 1989.

[12] C.-W. Shu and S. Osher. Efficient implementation of essentially non-oscillatory shock capturing schemes. *Journal of Computational Physics*, 77(2):439–471, 1988. ISSN 00219991. doi: 10.1016/0021-9991(89)90222-2.

[13] E. Weinan and C W Shu. A numerical resolution study of high order essentially non-oscillatory schemes applied to incompressible flow, 1994. ISSN 00219991.

[14] X Liu, S Osher, and T Chan. Weighted essentially non-oscillatory schemes, 1994. ISSN 00219991.

[15] G.-S. Jiang and C.-W. Shu. Efficient Implementation of Weighted ENO Schemes. 228(126):202–228, 1995.

[16] C K W Tam and J C Webb. Dispersion-relation-preserving finite difference schemes for computational acoustics, 1993. ISSN 00219991.

[17] M. P. Martín, E. M. Taylor, M. Wu, and V. G. Weirs. A bandwidth-optimized WENO scheme for the effective direct numerical simulation of compressible turbulence. *Journal of Computational Physics*, 220(1):270–289, 2006. ISSN 00219991. doi: 10.1016/j.jcp.2006.05.009.

[18] N Adams and K Shariff. A High-Resolution Hybrid Compact-ENO Scheme for Shock-Turbulence Interaction Problems. *Journal of Computational Physics*, 127 (1):27–51, 1996. ISSN 00219991. doi: 10.1006/jcph.1996.0156.

[19] Y X. Ren, M. Liu, and H Zhang. A characteristic-wise hybrid compact-WENO scheme for solving hyperbolic conservation laws. *Journal of Computational Physics*, 192(2):365–386, 2003. ISSN 00219991. doi: 10.1016/j.jcp.2003.07.006.

[20] A K. Henrick, T D. Aslam, and J M. Powers. Mapped weighted essentially non-oscillatory schemes: Achieving optimal order near critical points. *Journal of*

Computational Physics, 207(2):542–567, 2005. ISSN 00219991. doi: 10.1016/j.jcp.2005.01.023.

[21] Xuliang Liu, Shuhai Zhang, Hanxin Zhang, and Chi Wang Shu. A new class of central compact schemes with spectral-like resolution II: Hybrid weighted nonlinear schemes. *Journal of Computational Physics*, 284:133–154, 2015. ISSN 10902716. doi: 10.1016/j.jcp.2014.12.027. URL

.

[22] J H. Ferziger and M Peric. *Computational Methods for Fluid Dynamics*. 2002. ISBN 3540420746. doi: 10.1016/S0898-1221(03)90046-0.

[23] J B. Freund, P Moin, and S K. Lele. Compressibility effects in a turbulent annular mixing layer. Part 2. Mixing of a passive scalar. *J. Fluid Mech.*, 421(2000):269–292, 2000. ISSN 00221120. doi: 10.1017/S0022112000001634.

[24] F. A. Williams. Turbulent Combustion. In *The Mathematics of Combustion*, pages 97–131. 1985. ISBN 978-0-89871-053-3. doi: 10.1137/1.9781611971064.ch3.

[25] N Peters. Turbulent Combustion. *Measurement Science and Technology*, 12(11):2022–2022, 2001. ISSN 0957-0233. doi: 10.1088/0957-0233/12/11/708.

[26] S M Ghiaasiaan. *Convective Heat and Mass Transfer:*. Cambridge University Press, Cambridge, 2011. ISBN 9780511800603. doi: 10.1017/CBO9780511800603.

[27] M Gloor, D Obrist, and L Kleiser. Linear stability and acoustic characteristics of compressible, viscous, subsonic coaxial jet flow. *Physics of Fluids*, 25(8), 2013. ISSN 10706631. doi: 10.1063/1.4816368.

[28] J Fröhlich, Kuerten, B J. Geurts, and V Armenio. Simulation and Modeling of Turbulent Jet noise. *ERCOFTAC Series*, 20:305–310, 2015. ISSN 22151826. doi: 10.1007/978-3-319-14448-1.

[29] J. Hussein, S P. Capp, and W K. George. Velocity measurements in a high-Reynolds-number, momentum-conserving, axisymmetric, turbulent jet. *Journal of Fluid Mechanics*, 258(1994):31–75, 1994. ISSN 0022-1120. doi: 10.1017/S002211209400323X.

[30] I. Wygnanski and H. Fiedler. Some measurements in the self-preserving jet. *Journal of Fluid Mechanics*, 38(03):577, 1969. ISSN 0022-1120. doi: 10.1017/S0022112069000358.

[31] S B Pope. *Turbulent Flows*, volume 1. 2000. ISBN 0521598869. doi: 10.1088/1468-5248/1/1/702.

[32] F De Gregorio. Free compressible jet investigation. *Experiments in Fluids*, 55(3), 2014. ISSN 07234864. doi: 10.1007/s00348-014-1693-9.

[33] B J Boersma. A 6th order staggered compact finite difference method for the incompressible Navier-Stokes and scalar transport equations. *Journal of Computational Physics*, 230(12):4940–4954, 2011. ISSN 00219991. doi: 10.1016/j.jcp.2011.03.014.

[34] J. L. Stromberg, D K. McLaughlin, and T R. Troutt. Flow field and acoustic properties of a Mach number 0.9 jet at a low Reynolds number. *Journal of Sound and Vibration*, 72(2):159–176, 1980. ISSN 0022460X. doi: 10.1016/0022-460X(80)90650-1.

[35] S K. Lele. Compact finite difference schemes with spectral-like resolution. *Journal of Computational Physics*, 103(1):16–42, 1992. ISSN 10902716. doi: 10.1016/0021-9991(92)90324-R.

[36] R S. Hirsh. Higher order accurate difference solutions of fluid mechanics problems by a compact differencing technique. *Journal of Computational Physics*, 19(1):90–109, 1975. ISSN 10902716. doi: 10.1016/0021-9991(75)90118-7.

[37] Y Adam. Highly accurate compact implicit methods and boundary conditions. *Journal of Computational Physics*, 24(1):10–22, 1977. ISSN 10902716. doi: 10.1016/0021-9991(77)90106-1.

[38] K Mahesh. A Family of High Order Finite Difference Schemes with Good Spectral Resolution. *Journal of Computational Physics*, 145(332):332–358, 1998. ISSN 00219991. doi: 10.1006/jcph.1998.6022.

[39] R. W C P Verstappen and A. E P Veldman. Symmetry-preserving discretization of turbulent flow. *Journal of Computational Physics*, 187(1):343–368, 2003. ISSN 00219991. doi: 10.1016/S0021-9991(03)00126-8.

[40] C W Shu. Essentially Non-Oscillatory and Weighted Essentially Non-Oscillatory Schemes for Hyperbolic Conservation Laws. *ICASE Report*, (97-65):1–78, 1997. doi: 10.1007/BFb0096355.

[41] C W Shu. Chapter 4: Essentially non-oscillatory and weighted essentially non-oscillatory schemes for hyperbolic conservation laws. *Advanced Numerical Approximation of Nonlinear Hyperbolic Equations*, 1697:325–432, 1998. doi: 10.1007/BFb0096351.

[42] S Pirozzoli. Conservative Hybrid Compact-WENO Schemes for Shock-Turbulence Interaction. *Journal of Computational Physics*, 178(1):81–117, 2002. ISSN 00219991. doi: 10.1006/jcph.2002.7021.

[43] X. Y. Hu, Q. Wang, and N. A. Adams. An adaptive central-upwind weighted essentially non-oscillatory scheme. *Journal of Computational Physics*, 229(23): 8952–8965, 2010. ISSN 00219991. doi: 10.1016/j.jcp.2010.08.019.

[44] D F. Griffiths and D J. Higham. *Numerical Methods for Ordinary Differential Equations*, volume 79. 2010. ISBN 978-0-85729-147-9. doi: 10.1007/978-0-85729-148-6.

[45] J C Butcher. *Numerical Methods for Ordinary Differential Equations*. 2008. ISBN 9780470753767. doi: 10.1002/9780470753767.

[46] T. J. Poinsot and S. K. Lele. Boundary conditions for direct simulations of compressible viscous flows. *Journal of Computational Physics*, 101(1):104–129, 1992. ISSN 10902716. doi: 10.1016/0021-9991(92)90046-2.

[47] C M Ho and N S. Nosseir. Dynamics of an impinging jet. Part 1. The feedback phenomenon. *Journal of Fluid Mechanics*, 105(-1):119, 1981. ISSN 0022-1120. doi: 10.1017/S0022112081003133.

[48] D Bechert. Excitation of instability waves in free shear layers. Part 1. Theory. *J. Fluid Mech.*, 186:47–62, 1988. ISSN 0022-1120. doi: 10.1017/S0022112088000035.

[49] S. A. Orszag, M. Israeli, and H O Kreiss. Numerical simulation of viscous incompressible flows. *Annual Review of Fluid Mechanics*, 6:281–318, 1974. ISSN 0066-4189. doi: 10.1146/annurev.fl.06.010174.001433.

[50] P Dutt. Stable Boundary Conditions and Difference Schemes for NavierStokes Equations. *SIAM Journal on Numerical Analysis*, 25(2):245–267, 1988. ISSN 0036-1429. doi: 10.1137/0725018.

[51] K W Thompson. Time-dependent boundary conditions for hyperbolic systems, {II}. *Journal of Computational Physics*, 89:439–461, 1990. ISSN 00219991. doi: 10.1016/0021-9991(90)90152-Q.

[52] C Bogey and C Bailly. Three dimensional non reflective boundary conditions for acoustic simulations - far field formulation and validation test cases. *Acta*, 88: 463–471, 2002. ISSN 1436-7947.

[53] T Colonius, S K Lele, and P Moin. Boundary conditions for direct computation of aerodynamic sound generation. *AIAA Journal*, 31(9):1574–1582, 1993. ISSN 0001-1452. doi: 10.2514/3.11817.

[54] C Tam and Z Dong. Radiation and outflow boundary conditions for direct computation of acoustic and flow disturbances in a nonuniform mean flow. *Journal of Computational Acoustics*, 4(2):175–201, 1996.

[55] S Tan, C Wang, C W Shu, and J Ning. Efficient implementation of high order inverse Lax-Wendroff boundary treatment for conservation laws. *Journal of Computational Physics*, 231(6):2510–2527, 2012. ISSN 00219991. doi: 10.1016/j.jcp.2011.11.037.

[56] S Gottlieb and C W Shu. Total variation diminishing Runge-Kutta schemes. *Mathematics of Computation of the American Mathematical Society*, 67(221):73–85, 1998. ISSN 0025-5718. doi: 10.1090/S0025-5718-98-00913-2.

[57] A Michalke. Survey on jet instability theory, 1984. ISSN 03760421.

[58] N R Panchapakesan and J L Lumley. Turbulence measurements in axisymmetric jets of air and helium. Part 1. Air jet. *Journal of Fluid Mechanics*, 246(-1):197, 1993. ISSN 0022-1120. doi: 10.1017/S0022112093000096.

[59] D J. Bodony and S K. Lele. On using large-eddy simulation for the prediction of noise from cold and heated turbulent jets. *Physics of Fluids*, 17(8):1–20, 2005. ISSN 10706631. doi: 10.1063/1.2001689.

[60] I. Danaila and B. J. Boersma. Mode interaction in a forced homogeneous jet at low Reynolds numbers. In *Center for Turbulence Research - Proceedings of the Summer Program Program 1998*, pages 141–158, 1998. ISBN 0030-8870. doi: 10.1016/j.aqpro.2013.07.003.

[61] I Danaila, J Dušek, and F Anselmet. Coherent structures in a round, spatially evolving, unforced, homogeneous jet at low Reynolds numbers. *Physics of Fluids*, 9(11):3323–3342, 1997. ISSN 1070-6631. doi: 10.1063/1.869446.